Liouvillian and Hamiltonian exceptional points of atomic vapors: The spectral signatures of quantum jumps

Marek Kopciuch [*] and Adam Miranowicz [†]
Institute of Spintronics and Quantum Information, Faculty of Physics and Astronomy, Adam Mickiewicz University, 61-614 Poznań, Poland

(Received 3 June 2025; accepted 24 July 2025; published 22 August 2025)

We investigate spectral singularities in an alkali-metal atomic vapor modeled using four and effectively three hyperfine states. By comparing the eigenvalue spectra of a non-Hermitian Hamiltonian (NHH) and a Liouvillian superoperator, we analyze the emergence and characteristics of both semiclassical and quantum exceptional points. Our results reveal that, for atomic systems, the NHH approach alone may be insufficient to fully capture the system's spectral properties. While NHHs can yield accurate predictions in certain regimes, a comprehensive description typically requires the Liouvillian formalism, which governs the Lindblad master equation and explicitly incorporates quantum-jump processes responsible for repopulation dynamics. We demonstrate that the inclusion of quantum jumps fundamentally alters the spectral structure of the system. In particular, we present examples in which the existence, location in parameter space, or even the order of spectral degeneracies differs significantly between the two approaches, thereby highlighting the impact of quantum jumps and the limitations of the NHH method. Finally, using the hybrid-Liouvillian formalism, we show how quantum jumps reshape spectral features initially predicted by the NHH, ultimately determining the full Liouvillian spectrum.

DOI: 10.1103/zxw5-nlsn

I. INTRODUCTION

Non-Hermitian quantum physics has recently attracted considerable attention for its ability to describe energy dissipation in open quantum systems and to predict exotic phenomena such as exceptional points (EPs)—non-Hermitian degeneracies first studied in the 1960s [1]. However, intense research into EPs began in the early 2000s [2–4], spurred in part by the introduction of $\mathcal{PT}$-symmetric quantum mechanics based on non-Hermitian Hamiltonians (NHHs) [5,6].

Numerous studies investigating NHHs and their singularities, often termed Hamiltonian EPs (HEPs), in engineered non-Hermitian systems have emerged across a wide range of fields, as reviewed in Refs. [7–10]. These include optics [10–18], electronics [19], plasmonics [20–22], acoustics [23–28], cavity optomechanics [24,29–32], atom optics [33], circuit quantum electrodynamics (QED) [34–36], and cavity QED [37–39]. A variety of physical platforms have been employed in these investigations, such as photonic [13–16,40] and atomic [33] lattices, metamaterials [41–45], exciton-polariton systems [46], atomic vapors [47], trapped ions [48], or thermal atomic ensembles [49]. Numerous proposed applications of EPs span a wide range of fields, including [8,9] quantum control and state engineering, quantum thermodynamics, mode conversion and switching, topological energy transfer, dynamic stability control, and non-Hermitian quantum information processing, as well as neuromorphic and reservoir computing. Considerable attention has been directed toward signal amplification and spectral filtering near EPs, particularly for their potential use in exceptional-point-enhanced quantum sensing [50–52].

Effective NHHs can accurately describe coherent, nonunitary dynamics in classical and semiclassical systems. However, they fall short in capturing the full behavior of quantum systems subject to quantum jumps and associated noise corresponding to the loss or gain of an excitation (like photons, phonons, or magnons) exchanged with the environment, which monitors (measures) the system. A fully quantum treatment is therefore required—typically formulated through a Liouvillian superoperator derived from a master equation, or equivalently, via Fokker-Planck or Heisenberg-Langevin equations.

To address the limitations of HEPs derived from NHHs, the concept of quantum Liouvillian exceptional points (LEPs) was introduced [53,54]. LEPs are defined as spectral degeneracies of Liouvillian superoperators, where both eigenvalues and eigenvectors coalesce, paralleling the notion of HEPs in NHHs. By incorporating quantum jumps explicitly, LEPs extend the applicability of the HEP framework, enabling a consistent and physically complete description of decoherence and noise in open quantum systems, while preserving the structure of canonical commutation relations.

For classical or semiclassical systems—where quantum jumps are negligible—HEPs and LEPs yield consistent predictions. However, in fully quantum systems, the presence of

[*]Contact author: marek.kopciuch@amu.edu.pl
[†]Contact author: adam.miranowicz@amu.edu.pl

quantum jumps can significantly modify the structure of EPs: They may generate, shift, or even eliminate EPs, or reduce their order, as shown in this work. It should be emphasized that quantum jumps (responsible for repopulation processes) are particularly important in the context of atomic ensembles, as they underlie one of the most widely used techniques in atomic physics, i.e., optical pumping [55].

The connection between HEPs and LEPs can be naturally elucidated—and even continuously interpolated—within the hybrid-Liouvillian formalism of Ref. [56], by postselecting experimental outcomes based on the number of quantum jumps. The two limiting cases correspond to lack of quantum jumps (recovering HEPs) and an arbitrary number of jumps (leading to LEPs).

It should be stressed that LEPs are embedded within the well-established formalism of open quantum systems, making their interpretation and computation more transparent and physically grounded. Unlike NHH-based approaches, which often require the computation of system-specific metrics to ensure physical validity—following the formalism of $\mathcal{PT}$-symmetric quantum mechanics [5,6,57]—the analysis of Liouvillians and their exceptional points relies solely on standard quantum mechanics. This eliminates the ambiguities and potential pitfalls of the NHH framework, which, although mathematically rich and conceptually intriguing [58–60], can lead to misleading or incorrect conclusions (like apparent violations of no-go quantum information theorems [57]) if applied imprecisely.

Until recently, most research on EPs has focused on HEPs in classical or semiclassical systems, but interest in LEPs of fully quantum systems has been steadily increasing after their introduction in 2019—particularly driven by recent experimental advances in circuit QED [35,36,61,62] and trapped ion platforms [63–65]. Proposed applications of LEPs include enhanced quantum sensing and precise dynamical control of quantum systems. Notably, LEPs play a significant role in quantum thermodynamics—for instance, they act as indicators of critical decay regimes in quantum thermal machines [66], and experimental findings suggest they may enhance the efficiency of quantum heat engines [61,64]. Nevertheless, a more comprehensive investigation of the role of LEPs in comparison to HEPs is needed to fully exploit their potential for emerging quantum technologies.

LEPs have also been proposed and studied in the context of non-Markovian processes [67]. However, the present work focuses on dissipative dynamics and the corresponding LEPs within the framework of the standard Lindblad master equation.

Moreover, we study only EPs, but it would be interesting to search for other types of spectral degeneracies, including diabolical points (defined by degenerate eigenvalues with the corresponding orthogonal eigenvectors) [68] and hybrid points, which are higher-order degeneracies combining properties of exceptional and diabolical points [69,70]. It is also worth noting that quantum exceptional, diabolical, and hybrid degeneracies can alternatively be characterized using the Heisenberg-Langevin formalism, as demonstrated in Refs. [71–74].

In this work, motivated by the experimental observation of HEPs in alkali-metal atomic vapors modeled with a few hyperfine states [49], we investigate the emergence of LEPs within the same framework—including its generalization to account for detunings—and compare these quantum LEPs with the corresponding HEPs predicted by the non-Hermitian Hamiltonian approach.

Alkali-metal atomic vapors represent one of the most versatile platforms in atomic optics and quantum technologies. These systems operate across a wide range of conditions, enabling the study of diverse quantum phenomena. In the ultracold regime, alkali atoms are essential for realizing Bose-Einstein condensates [75–77] and optical lattices [77,78], which enable implementations of various quantum information algorithms. In the opposite thermal limit, known as the hot-vapor regime, temperatures often exceed 100 °C, allowing operation in the spin-exchange relaxation-free (SERF) regime [79–81]. In this regime, rapid interatomic collisions suppress decoherence, enabling collective spin dynamics [80], extended coherence times, and the observation of many-body entanglement [81].

Lying between these ultracold and hot vapor regimes is the room-temperature domain, where alkali vapors confined in antirelaxation-coated cells (e.g., paraffin-coated) exhibit surprisingly long spin coherence times [82]. This regime has enabled the observation of a wide range of quantum effects, including coherent population trapping [83], spin squeezing [84], macroscopic entanglement [85,86], spin wave dynamics [86], and the generation of squeezed and entangled light modes [84,87].

Remarkably, the room-temperature and SERF regimes have also provided the foundation for developing ultrasensitive quantum sensors. These include magnetometers [88–90], atomic gyroscopes [90,91], and detectors for exotic physics, such as searches for dark matter [92,93]. The combination of long coherence times, collective quantum behavior, and accessible experimental setups makes alkali-metal vapors a powerful testbed for investigating EPs, particularly in the context of enhanced quantum sensing.

Specifically, we employ an effective four-level model (and its effective three-level version) to describe optical transitions between two hyperfine manifolds in atomic vapors, characterized by total angular momenta f (ground state) and F (excited state). Of particular interest is the minimal configuration that still captures the essential dynamical features—namely, the transition $f = 1 \rightarrow F = 0$. This simple model is sufficient to distinguish the interactions of atomic states with light of different polarizations.

To ensure that the model faithfully represents real atomic transitions, it is crucial to account for the characteristic timescales of the system. In typical experimental realizations, the excited-state relaxation time is several orders of magnitude shorter than the timescales governing ground-state evolution. This separation of timescales justifies a common approximation: eliminating the excited state to obtain an effective description of the ground-state dynamics.

While adiabatic elimination and direct computation under the assumption of negligible excited-state population are standard techniques for this reduction, in this work we adopt a more systematic approach. Specifically, we utilize the effective operator formalism for open quantum systems, as introduced in Ref. [94] and detailed in Sec. III. This method

allows for a controlled dimensionality reduction and is especially advantageous for systems with larger excited-state angular momentum.

The paper is organized as follows: In Sec. II, we review the essential formalisms and definitions of EPs associated with NHHs, quantum Liouvillians, and hybrid Liouvillians. Section III introduces an effective description of the slowly varying ground-state dynamics in our system. Section IV discusses the model without radio-frequency (RF) detunings in the context of both the NHHs and Liouvillian superoperators. In Sec. V, we examine a generalized model with an additional detuning of the RF magnetic field, in which the HEPs and LEPs exhibit significant differences. Technical details, including lengthy derivations and formulas, are provided in the Appendixes for the reader's convenience. We present our conclusions in Sec. VII.

II. QUANTUM AND SEMICLASSICAL EXCEPTIONAL POINTS: BASIC CONCEPTS

A key objective of this article is to compute and compare the differences between EPs arising from the non-Hermitian part of the system's Hamiltonian—which governs coherent yet dissipative dynamics—and those of the full Liouvillian, which additionally incorporates quantum jumps. Following Ref. [54], these Hamiltonian and Liouvillian EPs are commonly referred to as (semi)classical and quantum EPs, respectively. To this end, we begin by recalling the basic definitions.

Exceptional points are singularities in a system's parameter space where two or more eigenvalues, along with their corresponding eigenvectors, coalesce. Unlike conventional degeneracies, EPs involve not only eigenvalue coincidence but also a collapse of the eigenspace, resulting in linearly dependent eigenvectors.

EPs are a hallmark of non-Hermitian systems—i.e., systems exhibiting loss, gain, or other nonunitary dynamics. As such, their analysis requires consideration of either an NHH spectrum or the full Liouvillian superoperator via the Lindblad master equation:

$$\dot{\rho} = \mathcal{L}(\rho) = -i[\hat{H}, \rho] - \sum_{\mu} \left(\frac{1}{2}\{\hat{L}_{\mu}^{\dagger}\hat{L}_{\mu}, \rho\} - \hat{L}_{\mu}\rho\hat{L}_{\mu}^{\dagger} \right), \quad (1)$$

where $\mathcal{L}$ represents the Liouvillian superoperator acting on the density matrix and $\hat{L}_{\mu}$ denotes quantum-jump operators. The key distinction between these two approaches lies in the treatment of quantum jumps: While NHHs account for dissipative evolution, only the Liouvillian framework captures the stochastic repopulation effects associated with quantum jumps. Equation (1) can be rewritten by defining an effective NHH:

$$\hat{H}_{\text{NH}} = \hat{H} - \frac{i}{2}\sum_{\mu} \hat{L}_{\mu}^{\dagger}\hat{L}_{\mu}, \quad (2)$$

which leads to the following transformation:

$$-i[\hat{H}_{\text{NH}}, \rho] \equiv -i(\hat{H}_{\text{NH}}\rho - \rho\hat{H}_{\text{NH}}^{\dagger}) = [\hat{H}, \rho] - \frac{1}{2}\sum_{\mu}\{\hat{L}_{\mu}^{\dagger}\hat{L}_{\mu}, \rho\}. \quad (3)$$

It is important to note that the commutator here includes complex conjugation, which is typically omitted when $\hat{H}$ is a self-adjoint operator. This generalized formulation allows us to express the master equation as

$$\frac{\mathrm{d}\rho}{\mathrm{d}t} = \mathcal{L}(\rho) = -i[\hat{H}_{\text{NH}}, \rho] + \sum_{\mu} \hat{L}_{\mu}\rho\hat{L}_{\mu}^{\dagger}. \quad (4)$$

This expression underscores the fundamental difference between analyzing LEPs, which account for the complete quantum dynamics including quantum jumps, and HEPs, which reflect only the coherent yet dissipative evolution described by the NHH.

Even though these two approaches may seem difficult to compare—since there is an apparent discontinuity due to the presence or absence of quantum jumps—there exists a way to interpolate this transition. This can be achieved by following the hybrid-Liouvillian formalism [56]:

$$\begin{aligned}\mathcal{L}'(\rho) &= -i[\hat{H}, \rho] - \sum_{\mu}\left(\frac{1}{2}\{\hat{L}_{\mu}^{\dagger}\hat{L}_{\mu}, \rho\} - q\hat{L}_{\mu}\rho\hat{L}_{\mu}^{\dagger}\right) \\ &= -i[\hat{H}_{\text{NH}}, \rho] + q\sum_{\mu}\hat{L}_{\mu}\rho\hat{L}_{\mu}^{\dagger}, \end{aligned} \quad (5)$$

where q is the quantum-jump parameter. In this framework, one possible interpretation is that it corresponds to an experiment with postselection, where only trajectories without quantum jumps ($q = 0$) are considered. In this limit, the evolution is governed purely by the NHH. More generally, the hybrid Liouvillian can be understood as describing an experiment in which the selection process leading to postselection is imperfect. By continuously varying q from 0 to 1, one obtains a smooth and physically meaningful interpolation between the spectrum of the NHH and the full Liouvillian spectrum.

It is worth noting that computing the spectrum of a Hamiltonian—whether Hermitian or non-Hermitian—is relatively straightforward, as it involves diagonalizing a matrix whose dimension corresponds to that of the system's Hilbert space. In contrast, analyzing the spectrum of the Liouvillian superoperator poses additional challenges. As shown in Eq. (1), the superoperator $\mathcal{L}$ acts on the density matrix in a nontrivial way, rather than as a simple matrix-vector multiplication. Nevertheless, because $\mathcal{L}$ is a linear, completely positive, and trace-preserving map, it can be recast as a matrix acting on the vectorized space of operators—that is, as a linear operator on the Liouville space. This representation allows the use of standard linear algebra techniques, albeit in a space whose dimension is the square of the Hilbert space dimension.

Importantly, while the spectrum of an NHH can be computed using standard diagonalization techniques, it is often advantageous to express the Hamiltonian in the superoperator formalism. This facilitates a direct comparison with the Liouvillian spectrum and provides a systematic way to identify how quantum jumps influence the system's dynamics.

Since the Liouvillian is a superoperator—acting on operators rather than vectors—it can be viewed as an operator on an extended space, where elements are vectorized representations of $d \times d$ matrices. Here, d denotes the dimension of the system's Hilbert space. Crucially, the action of the Liouvillian is not restricted to physical density matrices, which

are Hermitian, positive semidefinite, and trace-one. As a result, its eigenvectors often correspond to matrices that do not represent valid physical states—they may be non-Hermitian or have nonunit trace. Nevertheless, these eigenvectors of a nonsingular Liouvillian (so except LEPs) span the space of all $d \times d$ matrices, forming a complete basis. This enables one to decompose any physical density matrix in terms of these eigenvectors, with each component evolving independently according to the corresponding eigenvalue of the Liouvillian. This decomposition mirrors the role played by the Hamiltonian eigenbasis in the unitary evolution of closed quantum systems, offering a powerful tool for analyzing open-system dynamics.

One can classify the behavior of Liouvillian eigenvectors based on their associated eigenvalues as follows (see, e.g., Refs. [62,95,96]): (1) If an eigenvalue of the Liouvillian is zero, the corresponding eigenvector represents a stationary state of the system, remaining unchanged under the Liouvillian evolution. (2) If an eigenvalue is purely imaginary, the corresponding eigenvector undergoes periodic, undamped evolution. (3) If an eigenvalue is real and negative, the corresponding eigenvector exhibits simple exponential damping. (4) If an eigenvalue is complex with a negative real part, the corresponding eigenvector undergoes damped oscillatory evolution, where the imaginary part determines the oscillation frequency and the real part sets the decay rate.

III. EFFECTIVE NON-HERMITIAN HAMILTONIAN FOR THE MODEL

We analyze the theoretical model presented in Ref. [49]. The system consists of a ground state with total angular momentum $f = 1$ and an excited state with $F = 0$. The system is subject to two magnetic fields: a static leading field along the $\vec{z}$ axis, characterized by an effective Larmor frequency Ω_L, and a perpendicular oscillating field of the form $B_{\mathrm{RF}} \cos(\omega_{\mathrm{RF}} t)\vec{x}$, which induces coupling with an effective RF Rabi frequency $J = \gamma_B B_{\mathrm{RF}}/\sqrt{2}$, where γ_B is the gyromagnetic ratio of the given state. Additionally, the system interacts with linearly polarized light with polarization π. This results in the following Hamiltonian:

$$\hat{H}_0 = \begin{pmatrix} \Omega_L & Jc_t & 0 & 0 \\ Jc_t & 0 & Jc_t & -\Omega_R \cos(\omega t) \\ 0 & Jc_t & -\Omega_L & 0 \\ 0 & -\Omega_R \cos(\omega t) & 0 & \omega_0 \end{pmatrix}, \quad (6)$$

where $c_t = \cos(\omega_{\mathrm{RF}} t)$, ω is the laser frequency, ω_0 is the transition frequency between the ground and excited states, and Ω_R is the Rabi frequency of the optical transition.

To eliminate the time dependence from the Hamiltonian, the authors of Ref. [49] first apply the standard optical rotating-wave approximation (RWA), followed by a secondary transformation at the magnetic Larmor frequency associated with the ground state. Alternatively, a generalized RWA can be used to obtain a compact form of this transformation (for details, see Appendix A 3). The transformed Hamiltonian takes the form

$$\hat{H} = \begin{pmatrix} -\delta & J & 0 & 0 \\ J & 0 & J & -\Omega_R \\ 0 & J & \delta & 0 \\ 0 & -\Omega_R & 0 & -\Delta \end{pmatrix}, \quad (7)$$

where $\delta = \omega_{\mathrm{RF}} - \Omega_L$, $\Delta = \omega - \omega_0$, and ω_0 is the excited-state energy. For convenience, we adopt the rescaling $J/2 \to J$ and $\Omega_R/2 \to \Omega_R$.

To simplify the analysis of the four-level system, we reduce it to an effective three-level system that captures only the slow ground-state dynamics. This reduction is performed using the effective operator formalism, which was introduced in Ref. [94], while the detailed calculations are provided in Appendix A. The essential components of the Hamiltonian relevant to this effective description are identified as follows:

$$\hat{H}_g = -\delta \hat{F}_z + J\sqrt{2}\hat{F}_x, \quad (8)$$

$$\hat{V}_+ = (\hat{V}_-)^\dagger = -\Omega_R |00\rangle\langle 10|, \quad (9)$$

$$\hat{H}_e = -\Delta |00\rangle\langle 00|, \quad (10)$$

where $\hat{H}_{g(e)}$ is the ground (excited) state Hamiltonian and $\hat{F}_i$ is the angular momentum operator along the i axis. Next, the spontaneous-emission Lindblad operator for polarization ε, as defined in Eq. (A9), takes the following form:

$$\hat{L}_\varepsilon^{\mathrm{sp}} = i\sqrt{\frac{\Gamma}{3}} |1\bar{\varepsilon}\rangle\langle 00|. \quad (11)$$

Using Eqs. (A2), (A10), and (A11), we obtain the NHH for the excited state and its inverse:

$$\hat{H}_{\mathrm{eNH}} = -\frac{2\Delta + i\Gamma}{2} |00\rangle\langle 00|,$$
$$\hat{H}_{\mathrm{eNH}}^{-1} = -\frac{4\Delta - 2i\Gamma}{\Gamma^2 + 4\Delta^2} |00\rangle\langle 00|. \quad (12)$$

From Eqs. (A3) and (A4), it follows that

$$\hat{H}_{\mathrm{eff}} = \hat{H}_g + \frac{4\Delta\Omega_R}{\Gamma^2 + 4\Delta^2} |10\rangle\langle 10|, \quad (13)$$

$$\hat{L}_{\mathrm{eff}}^{\varepsilon} = \frac{2\sqrt{\Gamma}\Omega_R}{\sqrt{3}(\Gamma - 2i\Delta)} |1\bar{\varepsilon}\rangle\langle 10|. \quad (14)$$

Substituting these results into Eq. (2), we obtain the effective NHH:

$$\hat{H}_{\mathrm{NH}} = \hat{H}_g - \frac{2i\Omega_R^2}{\Gamma - 2i\Delta} |10\rangle\langle 10| = \begin{pmatrix} -\delta & J & 0 \\ J & -\frac{2i\Omega_R^2}{\Gamma - 2i\Delta} & J \\ 0 & J & \delta \end{pmatrix}. \quad (15)$$

Finally, by assuming the light is resonant with the transition ($\Delta \to 0$), we recover Eq. (2) from Ref. [49].

IV. RF TUNED REGIME OF THE MODEL

Here, we present both analytical and numerical analyses of the simplified NHH model described by Eq. (15), assuming that the RF magnetic field is tuned to the Larmor frequency ($\delta = 0$). In the case of the NHH alone, our results are consistent with the reasoning presented in Ref. [49]. However, the

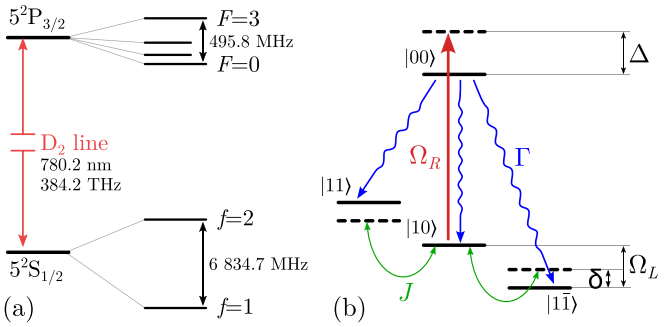

FIG. 1. (a) Energy-level diagram of the D_2 transition in ^{87}Rb, relevant for a potential experimental implementation of the studied system due to the presence of the $f = 1 \to F = 0$ transition. (b) Schematic of the relevant subspace spanned by the Zeeman sublevels. The red arrow indicates the optical transition, driven by a field with Rabi frequency Ω_R and detuning Δ. Blue wavy arrows represent spontaneous-emission channels associated with different photon polarizations, occurring at rate Γ. Green arrows depict radio-frequency (RF) magnetic coupling of strength J, detuned by δ from the Larmor frequency Ω_L.

inclusion of quantum jumps significantly alters the spectral properties, even in this simplified scenario.

A. Validation of the effective three-level model

At the beginning, we slightly depart from chronological order by first analyzing the Liouvillian of the full four-level system, obtained using the Liouville-Fock basis (see Appendix B 2), as well as that of the effective three-level system described by Eq. (27). This analysis is intended to demonstrate that the subsequent use of the effective model is fully justified within the parameter regime relevant for atomic vapor systems.

To rigorously compare the spectra, we performed numerical simulations using system parameters chosen within experimentally accessible ranges. In all cases, the spectra are governed by two parameters: the coupling strength of the oscillatory magnetic field (i.e., the magnetic field Rabi frequency, J) and the reduced optical Rabi frequency—Ω. The parameter Ω can be tuned by varying the coupling light intensity within the range from 1 μW to 10 mW, allowing for values in the range $10 < \Omega < 1000$.

It is important to note that the Liouvillian superoperator $\hat{\hat{\mathcal{L}}}$ depends on an additional parameter, Γ, which represents the natural linewidth (i.e., relaxation rate) of the excited state. For the experimentally employed D_2 transition (see the $F = 1 \to F = 0$ transition shown in Fig. 1) of ^{87}Rb, this parameter is given by $\Gamma = 2\pi \times 5.746$ MHz. One might also consider the $F = 1 \to F = 1$ transition present in the D_1 line, where $\Gamma = 2\pi \times 6.065$ MHz. However, as shown in the figures, this difference does not qualitatively affect the spectrum and has negligible quantitative impact on the part of the spectrum corresponding to the effective system.

An examination of Fig. 2(a) reveals a clear grouping of eigenvalues, which can be classified as $\lambda_i \approx 0$, $\Gamma/2$, or Γ. Specifically, the first group contains nine eigenvalues, the second group six, and the third group a single eigenvalue. This classification enables a straightforward physical interpretation: The first group corresponds to ground-state evolution, the second to ground-excited-state optical coherences, and the third to the excited state itself.

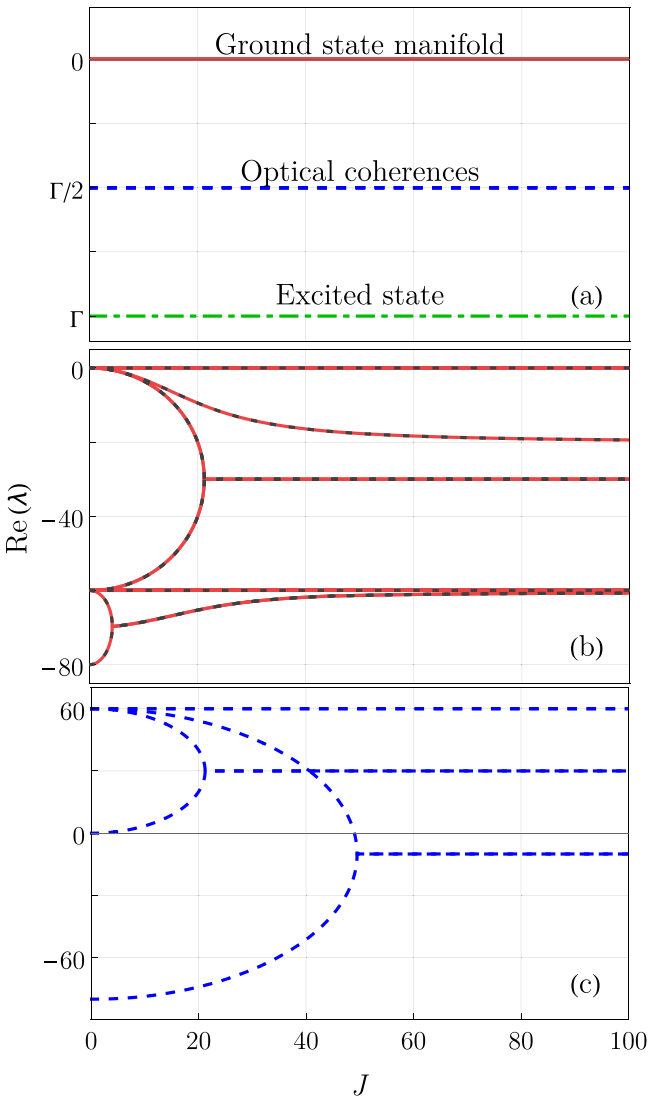

FIG. 2. Real part of the Liouvillian spectrum for the full four-level atomic system as a function of the coupling strength J calculated from Eq. (1) with Eqs. (7) and (11). Panel (a) presents the complete spectrum, while panels (b) and (c) provide magnified views of two spectrally distinct regions. These regions are identified based on their separation by characteristic spectral gaps: Panel (b) corresponds to the ground-state manifold and panel (c) to optical coherences. The excited-state contribution, consisting of a single level, is not magnified but remains visible in panel (a) as a green dash-dotted line. The color coding in panels (b) and (c) is consistent with that used in panel (a). The only distinction is that black dashed lines in panel (b) represent the spectrum of the effective ground-state Liouvillian as described by Eq. (27), illustrating the excellent agreement with the full system, with deviations not visible at the displayed scale. Note that the horizontal axis is shifted by $\Gamma/2$ in panel (b) and by Γ in panel (c) to better center the respective spectral regions. Assumed parameters: $\Gamma = 2\pi \times 5.7 \times 10^6$, $\Omega = 30$.

This also explains why small variations in Γ have little effect on the spectrum: The energy separation between these

groups is large compared to the internal dynamics within each group, rendering the system robust to minor changes in Γ.

B. Spectrum of the non-Hermitian Hamiltonian operator

Following the approach in Ref. [49], one can demonstrate that by setting both the optical field detuning Δ and the oscillating magnetic field detuning δ to zero, while also introducing the reduced Rabi frequency $\Omega = \Omega_R^2/\Gamma$, the Hamiltonian from Eq. (15) can be expressed as:

$$\hat{H}_{\text{NH}} = \begin{pmatrix} 0 & J & 0 \\ J & -2i\Omega & J \\ 0 & J & 0 \end{pmatrix}. \tag{16}$$

Its eigenvalues are readily obtained as

$$E_0 = 0, \quad E_\pm = -i\Omega \pm \sqrt{2J^2 - \Omega^2}, \tag{17}$$

with the corresponding eigenvectors given by

$$|E_0\rangle = -|11\rangle + |1\bar{1}\rangle, \tag{18}$$

$$|E_\pm\rangle = |11\rangle - \frac{i\Omega \pm \sqrt{2J^2 - \Omega^2}}{J}|10\rangle + |1\bar{1}\rangle. \tag{19}$$

From this expression, it becomes evident that when $2J^2 = \Omega^2$, the system exhibits a second-order HEP, characterized by the coalescence of both eigenvalues E_+ and E_-, as well as their corresponding eigenvectors. The reduced Rabi frequency was introduced to simplify the calculations; however, it is worth noting that it has a straightforward relation to, often used experimental parameter, the fine and hyperfine saturation parameters: $\kappa_1 = \Omega/\Gamma$ and $\kappa_2 = \Omega/\gamma$.

C. Additional isotropic relaxation

It is important to note that, up to this point, hyperfine isotropic relaxation has not been incorporated into our analysis. This aspect was likewise omitted in Ref. [49], where the authors acknowledged its relevance but did not explicitly include it in the NHH formulation. In our approach, this hyperfine relaxation is introduced in the form

$$\hat{L}^g_\mu \to \hat{L}^g_{mn} = \sqrt{\frac{\gamma}{3}}|1m\rangle\langle 1n|, \quad m, n = \{\pm 1, 0\}, \tag{20}$$

where γ is the rate of ground-state isotropic relaxation. This collection of relaxation channels results in isotropic relaxation [49]. To confirm this, we evaluate the corresponding effective relaxation operator (see Appendix A 4)

$$\hat{\Gamma} = \sum_{m,n} \left(\hat{L}^g_{mn}\right)^\dagger \hat{L}^g_{mn} = \frac{\gamma}{3}\sum_{m,n}|1n\rangle\langle 1m||1m\rangle\langle 1n| = \gamma\hat{1} \tag{21}$$

and the effective repopulation term (see Appendix A 4)

$$\begin{aligned}\hat{\Lambda}(\rho) &= \sum_{m,n}\hat{L}^g_{mn}\rho\left(\hat{L}^g_{m,n}\right)^\dagger \\ &= \frac{\gamma}{3}\sum_{m,n}|1m\rangle\langle 1n|\rho|1n\rangle\langle 1m| \\ &= \frac{\gamma}{3}\sum_n \rho_{nn}\hat{1} = \frac{\gamma}{3}\hat{1}.\end{aligned} \tag{22}$$

By incorporating these relaxation effects into Eq. (15), in accordance with Eq. (2) and under the previously stated assumptions, we arrive at the modified NHH:

$$\hat{H}^g_{\text{NH}} = \hat{H}_{\text{NH}} - i\hat{\Gamma} = \begin{pmatrix} -\frac{i\gamma}{2} & J & 0 \\ J & -\frac{i}{2}(\gamma + 4\Omega) & J \\ 0 & J & -\frac{i\gamma}{2} \end{pmatrix}. \tag{23}$$

This modification slightly alters the system's eigenenergies but does not affect its eigenstates. The resultant eigenvalues are

$$E_0 = -\frac{i\gamma}{2}, \tag{24}$$

$$E_\pm = -\frac{i}{2}(\gamma + 2\Omega) \pm \sqrt{2J^2 - \Omega^2}. \tag{25}$$

Since such isotropic relaxation does not significantly alter the spectral characteristics—producing only an overall isotropic shift—we omit it in the subsequent analysis. (The details of how isotropic relaxation modifies the superoperator spectrum are shown in Appendix C). Finally, we emphasize a subtle but important difference between the relaxation model assumed in our approach and that presented in the primary formulation of Ref. [49]. Specifically, in our treatment, only the ground state is subject to isotropic relaxation, whereas the authors of Ref. [49] include relaxation of the excited state as well. It is worth noting, however, that this distinction is negligible for experimentally relevant parameters, since the spontaneous-emission rate Γ typically exceeds the hyperfine relaxation rate γ by 4–6 orders of magnitude.

D. Spectrum of the hybrid Liouvillian

In the next stage of analyzing the model without RF detuning, we present calculations for the hybrid-Liouvillian model, which enables a fully quantum description of the system's evolution by explicitly incorporating quantum jumps, as described in Eq. (5). As a first step, we neglect hyperfine relaxation (see Appendix C), leading to

$$\hat{\hat{\mathcal{L}}}(q) = -i\hat{\hat{H}}_{\text{NH}} + q\hat{\hat{\Lambda}}_{\text{sp}}, \tag{26}$$

where $\hat{\hat{\Lambda}}_{\rm sp}$ represents the quantum jumps induced by spontaneous emission. As a result, the Liouvillian takes the following matrix form:

$$\hat{\hat{\mathcal{L}}}(q)=\begin{pmatrix} -2\Omega & 0 & 0 & 0 & J & 0 & 0 & 0 & 0 \\ 0 & -2\Omega & -2J & -J & 0 & 0 & 0 & 0 & 0 \\ 0 & 2J & -2\Omega & 0 & 0 & 0 & -J & \frac{2\Omega}{\sqrt{3}} & \sqrt{\frac{8}{3}}\Omega \\ 0 & J & 0 & 0 & 0 & 0 & -J & 0 & 0 \\ -J & 0 & 0 & 0 & 0 & J & 0 & 0 & 0 \\ 0 & 0 & 0 & 0 & -J & -2\Omega & 0 & 0 & 0 \\ 0 & 0 & J & J & 0 & 0 & -2\Omega & -\sqrt{3}J & 0 \\ 0 & 0 & \frac{2\Omega}{\sqrt{3}} & 0 & 0 & 0 & \sqrt{3}J & -\frac{2}{3}\Omega & -\frac{2}{3}\sqrt{2}\Omega \\ 0 & 0 & -2\sqrt{\frac{2}{3}}\Omega(q-1) & 0 & 0 & 0 & 0 & \frac{2}{3}\sqrt{2}\Omega(q-1) & \frac{4}{3}\Omega(q-1) \end{pmatrix}. \tag{27}$$

Noting that the only distinction between the NHH and the Liouvillian lies in the parameter q, it can be observed that $\hat{\hat{\mathcal{L}}}$ closely resembles $\hat{\hat{H}}_{\rm NH}$. The only difference appears in the last row. This is expected, as the last row corresponds to the decay of the ninth component of the vectorized density matrix, which is proportional to identity. Since quantum jumps serve as a repopulation mechanism that ensures probability conservation during the evolution, the vanishing last row of the Liouvillian reflects this property.

The spectral analysis of this operator is particularly interesting, as its limits at $q=0$ and $q=1$ correspond to the spectra of the NHH superoperator and the Liouvillian, respectively:

$$\hat{\hat{\mathcal{L}}}(0)=-i\hat{\hat{H}}_{\rm NH} \quad \hat{\hat{\mathcal{L}}}(1)=\hat{\hat{\mathcal{L}}}. \tag{28}$$

We obtain the following spectrum of $\hat{\hat{\mathcal{L}}}'(q)$:

$$\Big\{0,-2\Omega,-\alpha_1^*,-\alpha_1^*,-\alpha_1,-\alpha_1, -\frac{\phi}{\sqrt[3]{\zeta}}+\sqrt[3]{\zeta}+\Omega(2q-9),\beta_+,\beta_-\Big\}, \tag{29}$$

where

$$\beta_\pm=\frac{\phi}{\sqrt[3]{\zeta}}\frac{1\pm i\sqrt{3}}{2}-\sqrt[3]{\zeta}\frac{1\mp i\sqrt{3}}{2}+\Omega(2q-9), \tag{30}$$

and $\alpha_n=\Omega+in\sqrt{2J^2-\Omega^2}$ and $\zeta=\sqrt{\nu^2+\phi^3}+\nu$, together with $\phi=54J^2+\Omega^2(-4q^2+18q-27)$ and $\nu=\Omega q[324J^2+\Omega^2(8q^2-54q+81)]$. A key observation is that the first six eigenvalues remain independent of the parameter q, demonstrating an exact correspondence between the NHH and the full Liouvillian. Furthermore, for $q=0$, the expression simplifies to $\zeta=(54J^2-27\Omega^2)^{3/2}$. This leads to the following spectrum of the NHH:

$$\{0,-2\Omega,-\alpha_1^*,-\alpha_1^*,-\alpha_1,-\alpha_1,-2\alpha_1,-2\alpha_1^*,-2\Omega\}, \tag{31}$$

which reveals the emergence of a third-order exceptional point (EP3) in the NHH (see Fig. 3), marked by the coalescence of the three highest eigenvalues and their associated eigenvectors at $J\approx 21.1$. At first glance, it may appear counterintuitive that transitioning to the superoperator formalism enhances the order of the EP from second to third. Although this behavior is not universal, it is well justified. The superoperator representation effectively enlarges the dimensionality of the system's state space, which can lead to higher-order spectral degeneracies. A detailed discussion of the relationship between the spectra of non-Hermitian Hamiltonians and their corresponding superoperators is provided in Appendix B 5.

E. The spectral role of quantum jumps

Analysis of the results shown in Fig. 4 suggests that the inclusion of quantum jumps effectively lifts degeneracies, re-

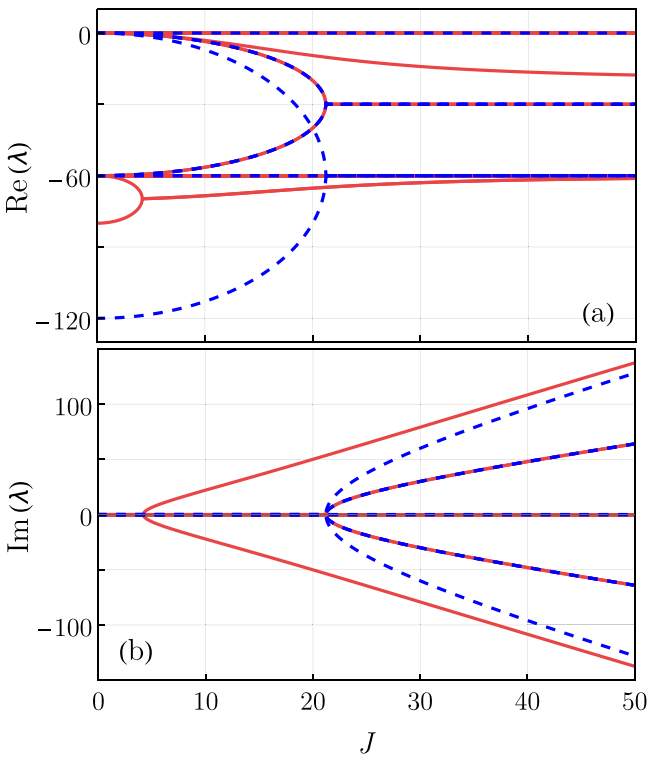

FIG. 3. Representative examples of the full spectra of the NHH superoperator (blue dashed curves) compared with those of the Liouvillian (red solid curves) as a function of J, obtained in the limits $q=0$ and 1 of Eq. (27), respectively. Note that the NHH superoperator corresponds to the hybrid Liouvillian in the limit of zero quantum-jump parameter ($q=0$). Panels (a) and (b) display the real and imaginary parts of the spectrum, respectively. We set $\Omega=30$.

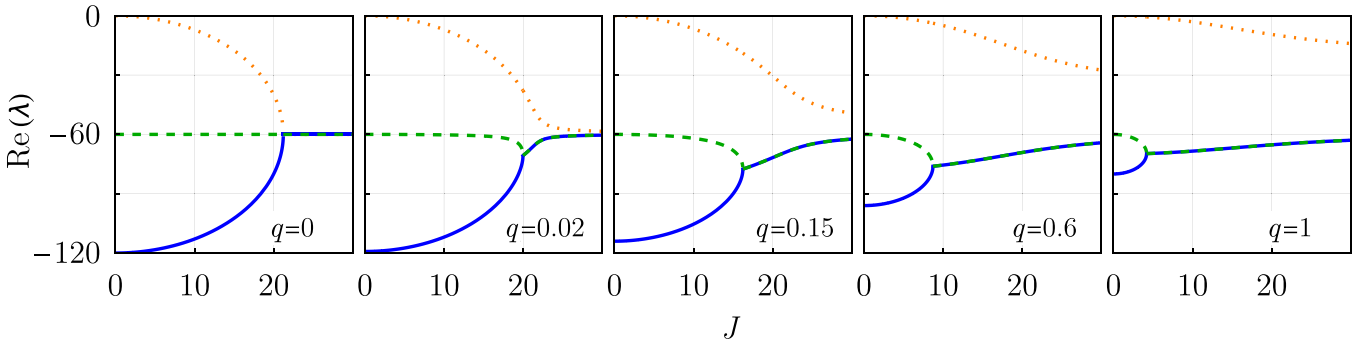

FIG. 4. Real part of the hybrid-Liouvillian spectra as a function of J, calculated from Eq. (27) for various values of the quantum-jump parameter q. The displayed eigenvalues correspond to those that form EP3 in the NHH limit. The plots illustrate how increasing q gradually lifts the spectral degeneracy, thereby modifying the spectrum. Different panels show results for q ranging from 0 (purely non-Hermitian case) to 1 (full Liouvillian case). We set $\Omega = 30$.

ducing the third-order HEP to a second-order LEP. To confirm this, one can calculate the quasienergy splitting of the eigenvalues as

$$\Delta E^R_{ij} = \mathrm{Re}(\lambda'_i - \lambda'_j), \quad \Delta E^I_{ij} = \mathrm{Im}(\lambda'_i - \lambda'_j). \tag{32}$$

Since the spectra of both the Liouvillian and hybrid Liouvillian are generally complex—reflecting the non-Hermitian nature of these superoperators—it is essential to analyze the real and imaginary parts of the quasienergy splitting separately.

Particularly interesting is the analysis of the three eigenvalues $\lambda_{7,8,9}$ that form the EP3. From Fig. 5, it is evident that $\Delta E^{R(I)}_{89}$ reaches zero sharply around $J \approx 21.1$. In contrast, the behavior of $\Delta E^{R(I)}_{78}$ and $\Delta E^{R(I)}_{79}$ is less clear, as these appear to approach zero asymptotically. To confirm this trend, we evaluate the limit of ΔE^R_{ij} as $J \to +\infty$:

$$\lim_{J\to+\infty} \Delta E^R_{78} = \lim_{J\to+\infty} \Delta E^R_{79} = \tfrac{4}{3}\Omega q, \tag{33}$$

$$\lim_{J\to+\infty} \Delta E^R_{89} = 0. \tag{34}$$

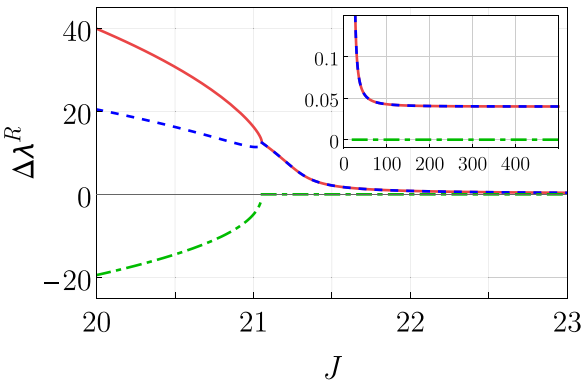

FIG. 5. Real and imaginary parts of the quasienergy splittings between the eigenvalues that originally formed the EP3 at $q = 0$, calculated from Eq. (27). The splittings shown are $\Delta\lambda^R_{89}$ (green dot-dashed curve), $\Delta\lambda^R_{79}$ (red solid curve), and $\Delta\lambda^R_{78}$ (blue dashed curve). The chosen value $q = 0.001$ demonstrates how even a small quantum-jump contribution lifts the degeneracy and reduces the EP order. The inset displays the real part of the splitting over a wider range of J, highlighting the asymptotic behavior. We set $\Omega = 30$.

This result confirms that even a small contribution of quantum jumps lifts the degeneracy of the third-order HEP. For the parameters used in Fig. 5, the asymptotic splitting is approximately 0.04.

F. Interpretation of the quantum-jump parameter

While the quantum-jump parameter q serves as a valuable mathematical tool that enables a smooth interpolation between the spectra of an NHH and the full Liouvillian superoperator, it also possesses a clear physical interpretation [35,56,97]. In the context of atomic vapors, this interpretation becomes evident from Fig. 6 and the structure of the master equation (1). As detailed in Appendix A 4, in atomic, molecular, and optical (AMO) physics, the final term in the master equation—associated with quantum jumps—is commonly referred to as the repopulation term, which ensures the preservation of the normalization of the reduced system's density matrix during open-system evolution.

From this perspective, the factor $(1 - q)$ quantifies the leakage of probability current into unobserved subspaces of the system. In the example shown in Fig. 6, this corresponds to population decay into the second spin manifold ($f = 2$), which remains unmonitored during the measurement process.

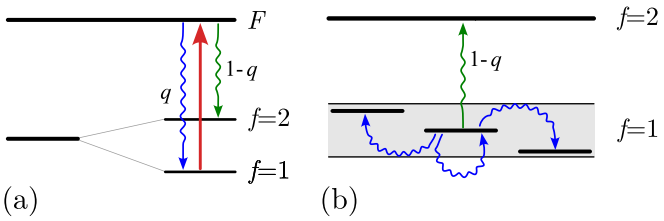

FIG. 6. Schematic illustration of the physical interpretation of the parameter q in the dynamics of atomic systems. (a) The full atomic level structure, where q denotes the fraction of the excited-state population that decays into the monitored manifold ($f = 1$), while the remaining fraction $(1 - q)$ decays into an unobserved manifold ($f = 2$). (b) An effective model in which the monitored manifold ($f = 1$) is treated as a reduced system. Here, $(1 - q)$ characterizes an effective population loss rate into the unobserved manifold ($f = 2$).

An analogous interpretation of q arises in quantum circuit dynamics experiments, where non-Hermitian evolution is typically engineered through postselection on quantum trajectories. In such settings, the parameter q effectively captures the detection efficiency—i.e., the likelihood of successfully monitoring quantum jumps. A value of $q < 1$ thus reflects imperfect detection or deliberate disregard of transitions into certain states considered as unobserved.

V. RF DETUNING REGIME OF THE MODEL

We consider a natural extension of the model of Ref. [49] for the $f = 1 \to F = 0$ transition, now assuming that the RF field is slightly detuned from exact resonance with the Larmor frequency. In any case, we continue to assume zero optical detuning. Since the physical system remains the same as described in Sec. III, we can directly apply Eq. (15) with $\Delta = 0$. Thus, we have

$$\hat{H}_{\rm NH} = \begin{pmatrix} \delta & J & 0 \\ J & -2i\Omega & J \\ 0 & J & -\delta \end{pmatrix}, \tag{35}$$

where δ denotes the detuning of the RF field from the Larmor frequency, introducing an additional degree of freedom for controlling and manipulating the system.

A. Spectrum of the Hamiltonian operator

A straightforward spectral analysis shows that the eigenvalues of the NHH are given by the roots of the characteristic polynomial:

$$x^3 + 2i\Omega x^2 - (2J^2 + \delta^2)x - 2i\Omega\delta = 0. \tag{36}$$

Analytical solutions to this cubic equation are generally not straightforward. However, with three adjustable parameters (Ω, J, and δ), one can tailor the system to exhibit specific spectral features. Notably, it is possible to realize a third-order degeneracy, where all three eigenvalues coalesce at a single point. To identify such a point, we assume the characteristic polynomial factorizes as $(x - ix_0)^3 = 0$. Given that the constant and quadratic terms in Eq. (36) are purely imaginary, the eigenvalues at this degeneracy must also be purely imaginary. This assumption leads to the following set of conditions:

$$x_0 = -\tfrac{2}{3}\Omega, \tag{37}$$

$$x_0^2 = \tfrac{1}{3}(2J^2 + \delta^2), \tag{38}$$

$$x_0^3 = -2\Omega\delta^2. \tag{39}$$

Solving this system of equations yields four solutions sharing the same quasienergy, given by $E_{\rm tp} = ix_0 = -2i\Omega/3$. Assuming $J > 0$ (since J represents the RF Rabi frequency), we also obtain two symmetric solutions for the detuning parameter:

$$\delta = \pm\frac{2}{3\sqrt{3}}\Omega, \quad J = \frac{4}{3\sqrt{3}}\Omega. \tag{40}$$

This symmetry reflects the system's invariance under reversal of the magnetic field, which corresponds to changing the sign of the detuning or, equivalently, exchanging the states $|0\rangle \leftrightarrow |2\rangle$ [see Fig. 1 and Eqs. (6) and (7)].

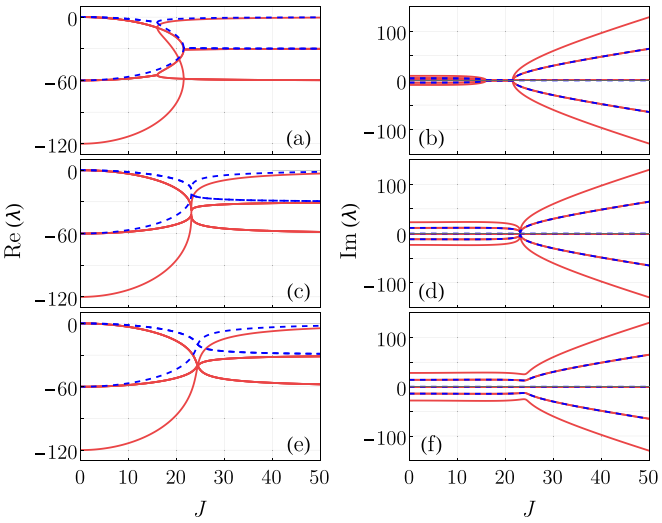

FIG. 7. Hamiltonian spectra of the three-level system as a function of the RF-field detuning δ from the Larmor frequency Ω_L. (a) and (b): $|\delta| < \delta_0 \equiv 2\Omega/(3\sqrt{3})$; (c) and (d): $|\delta| > \delta_0$; and (e) and (f): At the critical point $\delta = \delta_0$. Red curves show the spectra of the NHH superoperator [obtained from Eq. (27) in the limit $q = 0$], while blue dashed curves correspond to the spectra of the associated operator [calculated from Eq. (35)]. The left column presents the real part of the spectra, and the right column shows the imaginary part. Assumed parameters: $\Omega = 30$, with $\delta \approx 4.62$, 11.55, and 14, respectively.

Furthermore, it can be shown that within the detuning range $|\delta| < (2/3\sqrt{3})\Omega$, there exist two distinct values of J at which second-order degeneracy occurs, corresponding to a HEP, as discussed in detail in the next section. Outside this interval, no degeneracies are observed. This behavior demonstrates that by varying the RF-field detuning, it is possible to completely transform the system's characteristics—from having two second-order EPs (EP2), through a single third-order EP (EP3), to a regime where no exceptional points are observed (see Fig. 7).

An analysis of the eigenvector orthogonality confirms that all observed degeneracies correspond to EPs. In particular, at an EP3, all eigenstates coalesce into a single, parameter-independent eigenvector:

$$|E_{\rm tp}\rangle = \tfrac{1}{6}(\sqrt{3} + 3i)|1\bar{1}\rangle + \tfrac{1}{6}(\sqrt{3} - 3i)|10\rangle + \tfrac{1}{\sqrt{3}}|11\rangle. \tag{41}$$

B. Physical interpretation of the spectral regions

To elucidate the physical significance of these three regions, we examine the asymptotic behavior of the Hamiltonian in Eq. (35) and its influence on the real part of the spectrum. The regime $|\delta| < 2\Omega/(3\sqrt{3})$ is particularly revealing, as it features three distinct intervals in J, each corresponding to a different dominant dynamical behavior.

As shown in Fig. 8(a), for small values of J, the spectrum approaches that of the Hamiltonian $\hat{H}_{J\to 0} = \delta\hat{F}z$, where $\hat{F}_i$ is the angular momentum operator along the i axis. This indicates that the detuning term is dominant. In this regime, optical pumping (characterized by Ω) primarily influences the imaginary part of the spectrum, while the real part remains nearly unaffected. In the opposite limit ($J \to \infty$), the

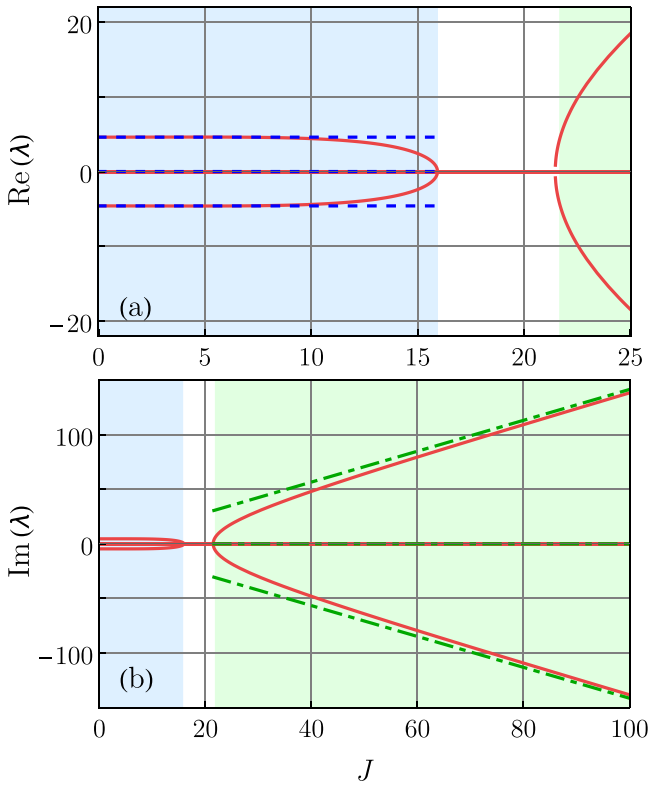

FIG. 8. (a) Real and (b) imaginary parts of the spectrum of the NHH operator (red solid curves), calculated from Eq. (27), illustrating the asymptotic behavior. The blue-shaded region ($J \to 0$) corresponds to the dynamics dominated by the $\delta \hat{F}_z$ term, where $\hat{F}_i$ is the angular momentum operator along the i axis, with the associated asymptote shown as a blue dashed line in panel (a). The green-shaded region ($J \to \infty$) reflects the dynamics governed by the $J\hat{F}_x$ term, with the corresponding asymptotes shown by green dot-dashed lines in panel (b). We set $\Omega = 30$ and $\delta = 4.62$.

spectrum converges to that of $\hat{H}_{J\to\infty} = J\hat{F}_x$, signifying that the RF field governs the system's dynamics.

The intermediate regime is more intricate. Previous analysis at $\delta = 0$ shows that a bifurcation emerges when $J \geqslant \Omega/\sqrt{2}$, marking the transition from optical-pumping-dominated behavior to RF-field dominance. Furthermore, the coupling parameter J links the dark states ($|11\rangle$ and $|1\bar{1}\rangle$) to the optically active state, thereby enhancing the influence of light and enabling it to affect not only the imaginary but also the real part of the spectrum. Finally, in the regime where the light-induced non-Hermitian component dominates, the eigenvalues are expected to be predominantly imaginary.

In summary, we conjecture that the three observed regions correspond to (1) a detuning-dominated regime, where δ exceeds the influence of both J and Ω; (2) a light-dominated regime, where J is small enough for optical effects to dominate over δ, yet not strong enough to suppress them; and (3) an RF-dominated regime, where J becomes sufficiently large to overpower both optical and detuning effects.

This framework also explains the absence of EPs in Fig. 7(c): The optical field is too weak relative to δ, and while a large J is needed to induce eigenvalue coalescence, such a value simultaneously suppresses all competing effects—including the optical ones.

C. Superoperator representation

The results presented here constitute a natural generalization of those in Sec. IV. As before, to facilitate a straightforward comparison between the full Liouvillian spectrum and that of the non-Hermitian Hamiltonian, we adopt the same hybrid-Liouvillian technique. Specifically, the hybrid Liouvillian introduced in Eq. (27) generalizes to

$$\hat{\hat{\mathcal{L}}}(q) = \begin{pmatrix} -2\Omega & -\delta & 0 & 0 & J & 0 & 0 & 0 & 0 \\ \delta & -2\Omega & -2J & -J & 0 & 0 & 0 & 0 & 0 \\ 0 & 2J & -2\Omega & 0 & 0 & 0 & -J & \frac{2\Omega}{\sqrt{3}} & 2\sqrt{\frac{2}{3}}\Omega \\ 0 & J & 0 & 0 & -2\delta & 0 & -J & 0 & 0 \\ -J & 0 & 0 & 2\delta & 0 & J & 0 & 0 & 0 \\ 0 & 0 & 0 & 0 & -J & -2\Omega & -\delta & 0 & 0 \\ 0 & 0 & J & J & 0 & \delta & -2\Omega & -\sqrt{3}J & 0 \\ 0 & 0 & \frac{2\Omega}{\sqrt{3}} & 0 & 0 & 0 & \sqrt{3}J & -\frac{2}{3}\Omega & -\frac{2}{3}\sqrt{2}\Omega \\ 0 & 0 & 2\sqrt{\frac{2}{3}}\Omega(q-1) & 0 & 0 & 0 & 0 & -\frac{2}{3}\sqrt{2}\Omega(q-1) & -\frac{4}{3}\Omega(q-1) \end{pmatrix}, \quad (42)$$

where a similar pattern of changes can be observed as in the previous case, particularly in the modification of the last row, which ensures the conservation of state normalization.

As in the case of the standard form of the detuned Hamiltonian, the general expressions for the quasienergies and eigenvectors are rather complicated and do not offer significant physical insight. However, as shown in previous section the standard form of the NHH reveals the existence of a particularly notable singularity within the three-dimensional parameter space Ω, δ, and J [see Eq. (40)], in which the EP3 arises. This point serves as a natural candidate for probing discrepancies between the NHH and the full Liouvillian descriptions, as the NHH superoperator is expected to inherit certain features from the standard-form dynamics. For these parameter values, the corresponding spectra are shown in Fig. 9. It can be observed that within the NHH superoperator description, the entire NHH spectrum collapses, with all nine eigenvalues becoming degenerate. Furthermore, the analysis

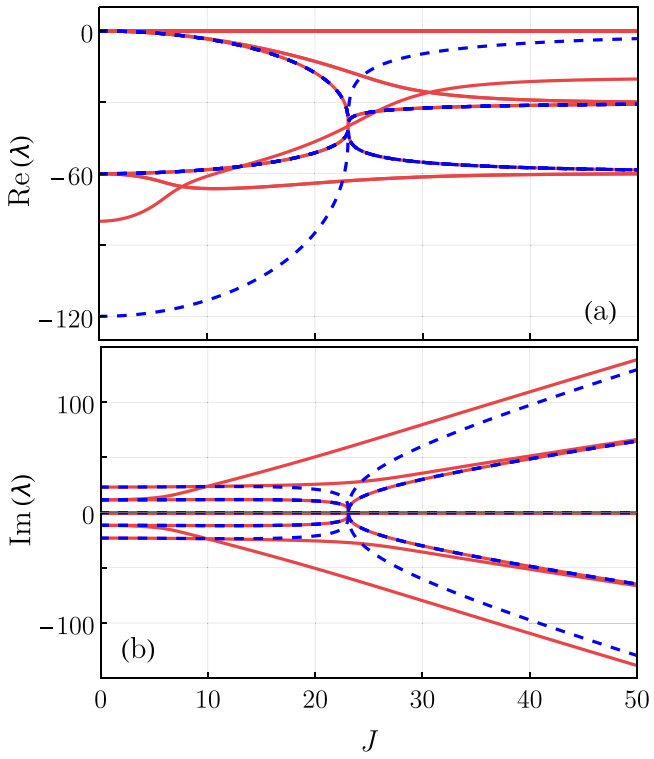

FIG. 9. (a) Real and (b) imaginary parts of the spectra of the Liouvillian (red solid curves) and the NHH (blue dashed curves) as a function of the coupling strength J, shown for parameters corresponding to the emergence of the EP3. The spectra correspond to the limits $q = 1$ and $q = 0$ of Eq. (42), respectively. This figure illustrates how the inclusion of quantum jumps modifies the spectrum and lifts the eigenvalue degeneracies. We set $\Omega = 30$ and $\delta \approx 11.55$.

of the Jordan chain reveals the presence of only three linearly independent eigenvectors, indicating the existence of at least two HEPs of orders 3 and 5. Introducing quantum jumps reduces the degeneracy order at this point significantly, demonstrating a marked decrease in the degree of degeneracy.

VI. PROPOSAL FOR EXPERIMENTAL OBSERVATION OF LIOUVILLIAN EXCEPTIONAL POINTS

In this subsection, we briefly outline possible methods for the experimental observation of the key results of our work—namely, the LEPs and their generalized forms, q-dependent LEPs, in the studied system.

Since LEPs correspond to singularities in the Liouvillian spectrum, the most natural and complete method for detecting them is to perform full quantum process tomography (QPT), which enables reconstruction of the entire Liouvillian superoperator. For systems with a few qubits implemented in superconducting quantum circuits, such a QPT-based approach was recently employed on the IBMQ platform to reveal single-qubit LEPs [62].

In our case, however, we consider atomic vapor systems and a qutrit (rather than a qubit). While the general concept remains the same, we propose to adopt a QPT method adapted to atomic vapors, based on quantum state tomography (QST) as introduced in Ref. [98] and experimentally implemented

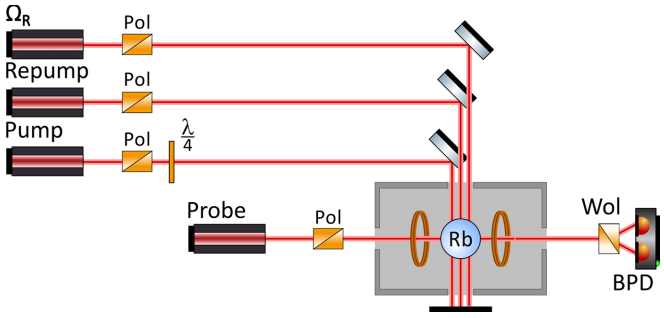

FIG. 10. Conceptual schematic of the experimental setup used for QPT in room-temperature atomic vapors, enabling the observation of LEPs and hybrid LEPs. Three laser beams—labeled Pump, Repump, and Probe—are used to implement the tomography protocol described in Refs. [99,102], which relies on FID-based state reconstruction [99]. An additional laser beam, denoted by Ω_R, provides the optical coupling required by the theoretical model. Optical components include Pol, a crystalline polarizer; $\lambda/4$, a quarter-wave plate; Wol, a Wollaston prism; and BPD, a balanced photodetector. The Rb cell refers to a paraffin-coated glass vapor cell containing rubidium-87, enclosed within a magnetically shielded environment.

in Ref. [99]. Figure 10 shows a simplified scheme of the experimental setup used for QST in Ref. [99].

To extend this QST protocol to full QPT, it is sufficient to apply QST to a complete set of input basis states. The experimental setup can remain unchanged from that in Fig. 10. For example, in the case of a qutrit, the basis states can be taken as eigenstates of the eight Gell-Mann matrices, which span the SU(3) algebra [100]. By performing QST on the output states corresponding to each of these basis inputs, full reconstruction of the Liouvillian becomes possible. One can then extract its eigenvalues and search for degeneracies using the same strategy as in Ref. [62].

Regarding the observation of hybrid Liouvillians, we note that several variants of QPT exist, including so-called Lindblad tomography, which enables separate reconstruction of the coherent (Hamiltonian) and incoherent (dissipator) parts of the dynamics. This method was demonstrated experimentally for reconstructing single- and two-qubit Lindbladians on a superconducting quantum processor in Ref. [101]. Through appropriate postprocessing of QPT data, it is possible to isolate the Lindblad dissipator and Hamiltonian contributions. By adjusting the statistical weight parameter q between them, hybrid Liouvillians can be constructed and analyzed.

An alternative, more direct route to observing system dynamics for a specific value of q is to engineer postselected trajectories. In optical systems, this is often simulated by adjusting detection efficiency using beam splitters or attenuators [56,97]. Another method is to monitor a specific dissipative channel via an ancillary detector and postselect only those measurement runs with a specified number of detected quantum jumps [35].

In the case of atomic vapors, where the measured signal contains ensemble-averaged information from many atoms, these jumps manifest as a reduction in the free-induction decay (FID) signal, including observable changes in absorption or polarization rotation. This becomes more intuitive upon realizing that the amplitude of the FID signal is proportional

to the number of atoms actively interacting with the light field [98]. Referring to Fig. 6, one can observe that jumps into the unobserved subspace reduce the number of atoms contributing to the measurable signal, thereby decreasing the FID amplitude in a detectable manner.

We propose applying a similar approach to our atomic vapor system by embedding the qutrit dynamics within a four-level (quartit) system. As illustrated in Fig. 6(b), the three lower levels—magnetic sublevels of the $f = 1$ hyperfine state—encode the qutrit states under investigation, while the fourth level serves as an effective decay channel.

To simulate the hybrid Liouvillian with $q = 0$ (corresponding to purely non-Hermitian dynamics), the experiment must be designed such that the excited state, to which the qutrit is optically coupled, cannot decay into the unobserved part of the system. A relevant example is the $f = 1 \to F = 0$ transition, where subsequent spontaneous decay from $F = 0$ to $f = 2$ is forbidden by selection rules. Intermediate values of q can be obtained by tuning the system to a different excited state, effectively modifying the relative transition strengths between the qutrit subspace ($f = 1$) and the auxiliary manifold ($f = 2$).

This approach enables the implementation of a conditional QPT protocol tailored for reconstructing hybrid Liouvillians. The experimental setup illustrated in Fig. 10 allows QPT to be performed across a tunable range of q values, with the atomic dynamics confined to the appropriate regime [see Fig. 1(b)]. In doing so, the methodology developed in Ref. [35] for superconducting quantum circuits is effectively adapted to room-temperature atomic vapor systems, paving the way for experimental exploration of both standard and hybrid LEPs in a qutrit.

VII. CONCLUSIONS

In this work, motivated by the theoretical and experimental results of Ref. [49], we have explored spectral singularities of their alkali-metal atomic vapor system (as shown in Fig. 1), modeled using four and effectively three hyperfine states, to investigate the nature of EPs in open quantum dynamics. By systematically comparing the spectra of NHHs and quantum Liouvillian superoperators, we identified significant discrepancies between semiclassical and fully quantum descriptions of dissipation, especially in the detuned system.

Our results demonstrate that while NHHs can approximate the system's behavior in limited regimes—particularly in the absence of quantum fluctuations—their predictive power breaks down when quantum-jump processes become significant. These jumps, intrinsic to the Lindblad framework, are responsible for state repopulation and fundamentally reshape the system's spectral features. This is particularly important for atomic systems with particle number conservation, where repopulation terms are unavoidable for an accurate description of the system. These terms give rise to many important phenomena, such as optical pumping [55].

We have presented concrete examples in which the presence or absence of EPs, their precise location in parameter space, or their algebraic multiplicity differ markedly between the NHH and Liouvillian approaches. These findings highlight that quantum jumps do not merely perturb the spectrum but may induce or destroy the order of degeneracies, altering the qualitative structure of the dynamics.

To bridge the gap between these two approaches, we employed the hybrid-Liouvillian formalism, which enables a controlled interpolation between the jump-free and fully stochastic regimes. This framework clarifies how spectral features predicted by NHHs evolve under the inclusion of quantum jumps, ultimately converging to the Liouvillian spectrum that governs fully quantum dynamics.

Regarding the experimental verification of the predicted Liouvillian EPs, this can be achieved indirectly by generalizing the approach of Ref. [49] or directly and comprehensively through quantum process tomography. The latter approach follows the method recently demonstrated in a circuit QED experiment [62]. In particular, the quantum state [98,99] and process [102] tomography techniques developed for alkali-metal atomic vapors could, in principle, be adapted to the system studied in Ref. [49].

Overall, our study reinforces the importance of Liouvillian-based methods for accurately capturing the spectral singularities of open quantum systems, particularly in effectively low-dimensional atomic platforms where quantum noise cannot be neglected. These insights are relevant for ongoing experimental efforts in quantum optics, quantum thermodynamics, and quantum sensing, where Liouvillian EPs offer both fundamental and practical significance.

ACKNOWLEDGMENTS

We gratefully acknowledge insightful discussions with Szymon Pustelny, Yujie Sun, and Arash Dezhang Fard. This work was supported by the Polish National Science Centre (NCN) under the Maestro Grant No. DEC-2019/34/A/ST2/00081.

DATA AVAILABILITY

No data were created or analyzed in this study.

APPENDIX A: EFFECTIVE SYSTEM DESCRIPTION

The calculation of effective dynamics can be challenging in certain cases. Here, we apply the method introduced in Ref. [94]. This formalism is valid under several key assumptions: (1) the system must exhibit Markovian dynamics, (2) be described within a Liouvillian framework, (3) feature a perturbative coupling between ground and excited states, and (4) display a clear separation of timescales—specifically, the relaxation of the excited state must occur much faster than the evolution within the ground-state manifold.

While the original formulation does not explicitly include the intrinsic, slow relaxation of the ground state, it can be naturally extended to incorporate this effect. In our system, we identify two distinct types of Lindblad operators. The first, $\hat{L}_\varepsilon^{\mathrm{sp}}$, represents spontaneous emission from the excited state with polarization $\varepsilon \in \pm 1, 0$. The second, $\hat{L}_\mu^g$, accounts for the intrinsic, slow relaxation processes within the ground-state manifold. Importantly, since $\hat{L}_\mu^g$ does not couple to the excited state, it remains unaffected by the effective operator formalism. In contrast, $\hat{L}_\varepsilon^{\mathrm{sp}}$ must be modified to reflect the ef-

fective dissipation in the ground state, arising from transitions through the excited state followed by spontaneous emission.

We begin by decomposing the system Hamiltonian as

$$\hat{H} = \hat{H}_g + \hat{H}_e + \hat{V}_+ + \hat{V}_-, \tag{A1}$$

where $\hat{H}_{g(e)} = \hat{P}_{g(e)}\hat{H}\hat{P}_{g(e)}$ represents the ground (excited) state Hamiltonian, obtained via the projection operators $\hat{P}$. Additionally, $\hat{V}_{+(-)} = \hat{P}_{e(g)}\hat{H}\hat{P}_{g(e)}$ corresponds to the generalized raising and lowering operators, respectively.

To formalize this approach, we introduce the effective non-Hermitian Hamiltonian governing the dynamics within the excited-state manifold as

$$\hat{H}_{\mathrm{eNH}} = \hat{H}_e - \frac{i}{2}\sum_{\varepsilon}\left(\hat{L}_{\varepsilon}^{\mathrm{sp}}\right)^{\dagger}\hat{L}_{\varepsilon}^{\mathrm{sp}}, \tag{A2}$$

where, following Ref. [55], the Lindblad operators are proportional to the electric-dipole-moment operator governing transitions between the ground and excited states, while also accounting for the directionality of the emission, since spontaneous emission cannot excite the atom—i.e., $\hat{L}_{\varepsilon}^{\mathrm{sp}} \propto \hat{P}_g\hat{d}_{\varepsilon}\hat{P}_e$. With this in mind, one can define the effective ground-state Hamiltonian and the effective spontaneous-emission Lindblad operators as

$$\hat{H}_{\mathrm{eff}} = -\tfrac{1}{2}\hat{V}_-\left[H_{\mathrm{eNH}}^{-1} + \left(\hat{H}_{\mathrm{eNH}}^{-1}\right)^{\dagger}\right]\hat{V}_+ + \hat{H}_g, \tag{A3}$$

$$\hat{L}_{\mathrm{eff}}^{\varepsilon} = \hat{L}_{\varepsilon}^{\mathrm{sp}}\hat{H}_{\mathrm{eNH}}^{-1}\hat{V}_+. \tag{A4}$$

It is worth noting that, in contrast to other methods, such an effective Hamiltonian does not require Hermitization to describe unitary evolution, as it is Hermitian *a priori*, while all effective dissipative processes are contained in $\hat{L}_{\mathrm{eff}}^{\varepsilon}$ and $\hat{L}_{\mu}^{g}$, resulting in the effective master equation or effective Liouvillian:

$$\begin{aligned}\dot{\rho}_g = \mathcal{L}_{\mathrm{eff}}(\rho_g) = &-i[\hat{H}_{\mathrm{eff}}, \rho_g] \\ &- \sum_{\varepsilon}\left(\frac{1}{2}\left\{\left(\hat{L}_{\mathrm{eff}}^{\varepsilon}\right)^{\dagger}\hat{L}_{\mathrm{eff}}^{\varepsilon}, \rho_g\right\} - \hat{L}_{\mathrm{eff}}^{\varepsilon}\rho_g\left(\hat{L}_{\mathrm{eff}}^{\varepsilon}\right)^{\dagger}\right) \\ &- \sum_{\mu}\left(\frac{1}{2}\left\{\left(\hat{L}_{\mu}^{g}\right)^{\dagger}\hat{L}_{\mu}^{g}, \rho_g\right\} - \hat{L}_{\mu}^{g}\rho_g\left(\hat{L}_{\mu}^{g}\right)^{\dagger}\right),\end{aligned} \tag{A5}$$

where ρ_g denotes the density matrix projected onto the Hilbert space of the ground-state manifold.

1. Spontaneous emission

As mentioned in the previous section, in the system of interest the only relaxation channel that couples the excited and ground states is spontaneous emission. Following Ref. [55], the Lindblad operators describing this process are proportional to the electric-dipole-moment operator governing transitions between the ground and excited states. They must also account for directionality, as spontaneous emission cannot excite the atom—i.e., $\hat{L}_{\varepsilon}^{\mathrm{sp}} \propto \hat{P}_g\hat{d}_{\varepsilon}\hat{P}_e$. In the case of a simple two-level system, the total relaxation rate Γ can be treated as an experimentally determined parameter, reducing the problem to finding the relative coupling strengths between different sublevels:

$$\begin{aligned}\hat{L}_{\varepsilon}^{\mathrm{sp}} &= \sum_{m,M}\frac{\sqrt{\Gamma}}{\langle f||\hat{d}||F\rangle}\langle fm|\hat{d}_{\varepsilon}|FM\rangle|fm\rangle\langle FM| \\ &= \sqrt{\Gamma}\sum_{m,M}\begin{pmatrix} f & 1 & F \\ -m & \varepsilon & M\end{pmatrix}|fm\rangle\langle FM|,\end{aligned} \tag{A6}$$

where we adopt the convention that lowercase (uppercase) letters denote ground (excited) states. In the first equation, the relaxation rate is rescaled by the reduced matrix element of the dipole operator, $\langle f||\hat{d}||F\rangle$, which arises naturally from the Wigner-Eckart theorem. This follows the convention in Ref. [55] and is expressed using the Wigner 3j symbol.

Since the reduced matrix element of $\hat{d}$ is not guaranteed to be positive, particular care must be taken when evaluating the Hermitian conjugate of the corresponding Lindblad operator:

$$\begin{aligned}\left(\hat{L}_{\varepsilon}^{\mathrm{sp}}\right)^{\dagger} &= \sum_{m,M}\frac{\sqrt{\Gamma}}{\langle f||\hat{d}||F\rangle}\langle FM|\hat{d}_{\varepsilon}^{\dagger}|fm\rangle|FM\rangle\langle fm| \\ &= \sum_{m,M}\frac{\sqrt{\Gamma}}{\langle f||\hat{d}||F\rangle}\langle FM|\hat{d}_{-\varepsilon}|fm\rangle|FM\rangle\langle fm| \\ &= \frac{\sqrt{\Gamma}\langle F||\hat{d}||f\rangle}{\langle f||\hat{d}||F\rangle}\sum_{m,M}\begin{pmatrix} F & 1 & f \\ -M & -\varepsilon & m\end{pmatrix}|FM\rangle\langle fm|.\end{aligned} \tag{A7}$$

By applying Eq. (10.27) from Ref. [55] together with the symmetry properties of the Wigner 3j symbol [103], we obtain

$$\begin{aligned}\left(\hat{L}_{\varepsilon}^{\mathrm{sp}}\right)^{\dagger} &= \sqrt{\Gamma}(-1)^{F-f}\sum_{m,M}\begin{pmatrix} F & 1 & f \\ -M & -\varepsilon & m\end{pmatrix}|FM\rangle\langle fm| \\ &= \sqrt{\Gamma}(-1)^{2F+1}\sum_{m,M}\begin{pmatrix} f & 1 & F \\ m & -\varepsilon & -M\end{pmatrix}|FM\rangle\langle fm| \\ &= \sqrt{\Gamma}(-1)^{F-f}\sum_{m,M}\begin{pmatrix} f & 1 & F \\ -m & \varepsilon & M\end{pmatrix}|FM\rangle\langle fm|.\end{aligned} \tag{A8}$$

This result introduces a subtle ambiguity because complex conjugation can alter the sign of a real-valued operator. This issue arises since the phase factor is effectively absorbed into the experimentally determined value of Γ. Notably, due to selection rules for optical transitions, $\Delta f = F - f$ takes values of ± 1 or 0. To resolve this ambiguity, we redefine the jump operators as follows:

$$\hat{L}_{\varepsilon}^{\mathrm{sp}} = i^{\Delta f}\sqrt{\Gamma}\sum_{m,M}\begin{pmatrix} f & 1 & F \\ -m & \varepsilon & M\end{pmatrix}|fm\rangle\langle FM|. \tag{A9}$$

This allows for a straightforward derivation of $(\hat{L}_{\varepsilon}^{\mathrm{sp}})^{\dagger}\hat{L}_{\varepsilon}^{\mathrm{sp}}$, which is useful, for example, in calculating the non-Hermitian Hamiltonian. Note that the above expression involves only the projection onto the excited state:

$$\left(\hat{L}_{\varepsilon}^{\mathrm{sp}}\right)^{\dagger}\hat{L}_{\varepsilon}^{\mathrm{sp}} = \Gamma\sum_{m,M}\begin{pmatrix} f & 1 & F \\ -m & \varepsilon & M\end{pmatrix}^2|FM\rangle\langle FM|. \tag{A10}$$

In the calculation of the non-Hermitian Hamiltonians $\hat{H}_{\mathrm{NH}}$ or $\hat{H}_{\mathrm{eNH}}$, we are especially interested in the collective effect

obtained by summing over all polarization components ε:

$$\sum_q \left(\hat{L}_q^{\rm sp}\right)^\dagger \hat{L}_q^{\rm sp} = \Gamma \sum_M \left(|FM\rangle\langle FM| \sum_{q,m} \begin{pmatrix} f & 1 & F \\ -m & q & M \end{pmatrix}^2 \right) = \frac{\Gamma}{2F+1} \sum_M |FM\rangle\langle FM| = \frac{\Gamma}{2F+1} \hat{P}_e, \tag{A11}$$

where we have used one of the summation rules for the Wigner 3j symbol over magnetic sublevels [103].

2. Raising and lowering operators

It is important to note that, in the model under consideration, the primary mechanism coupling the ground and excited states is an external light beam. Mathematically, this coupling closely resembles the spontaneous-emission jump operator, as both processes are governed by the same electric-dipole-moment operator, $\hat{d}_\varepsilon$. Moreover, we treat the coupling light beam as a classical field, which leads to the introduction of an interaction term in the Hamiltonian, expressed as

$$\hat{H}_E = -\vec{E} \cdot \hat{\vec{d}} \cos(\omega t), \tag{A12}$$

where $\vec{E} = E_0 \hat{e}$ represents the electric field vector of the light beam, with amplitude E_0 and unit vector $\hat{e}$, while ω is the carrier frequency.

Since the optical frequency is typically several orders of magnitude higher than any other relevant frequency in the system, the RWA naturally applies [55]. For a simple two-level system, the transformation between the static and rotating frames is given by

$$\hat{U}_{\rm rwa} = \hat{P}_g + \hat{P}_e e^{-i\omega t}. \tag{A13}$$

Under this transformation, the Hamiltonian takes the form

$$\hat{\tilde{H}} = \hat{U}_{\rm rwa}^\dagger \hat{H} \hat{U}_{\rm rwa} - i\hbar \hat{U}_{\rm rwa}^\dagger \frac{\partial}{\partial t} \hat{U}_{\rm rwa} = \hat{U}_{\rm rwa}^\dagger \hat{H} \hat{U}_{\rm rwa} - \hat{P}_e \hbar\omega. \tag{A14}$$

This results in a simplified form of Eq. (A12), which reads

$$\hat{H}_E = -\frac{1}{2} \vec{E} \cdot \hat{\vec{d}} - \hat{P}_e \hbar\omega = -\frac{E_0}{2} \sum_\varepsilon \hat{e}_\varepsilon \hat{d}_\varepsilon - \hat{P}_e \hbar\omega. \tag{A15}$$

For further details, see Ref. [55]. For simplicity, we omit the tilde notation for transformed operators and refer to the RWA only in the text.

To explicitly express this interaction, it is useful to apply the Wigner-Eckart theorem. Moreover, since the dipole operator $\hat{d}$ is an odd operator, it couples only ground and excited states without inducing additional energy shifts. By applying $\hat{V}_+ = \hat{P}_e \hat{H}_E \hat{P}_g$, we then obtain

$$\begin{aligned} \hat{V}_+ &= -\frac{E_0}{2} \sum_{m,M} \langle FM| \sum_\varepsilon \hat{e}_\varepsilon \hat{d}_\varepsilon |fm\rangle |FM\rangle\langle fm| \\ &= -\frac{E_0}{2} \langle F||\hat{d}||f\rangle \sum_{\varepsilon,m,M} \hat{e}_\varepsilon \bar{1}^{F-M} \begin{pmatrix} F & 1 & f \\ \bar{M} & \varepsilon & m \end{pmatrix} |FM\rangle\langle fm| \\ &= \Omega_R \sum_{\varepsilon,m,M} \hat{e}_\varepsilon \bar{1}^{F-M} \begin{pmatrix} F & 1 & f \\ \bar{M} & \varepsilon & m \end{pmatrix} |FM\rangle\langle fm|, \end{aligned} \tag{A16}$$

where Ω_R denotes the Rabi frequency, and for compactness, we use the notation $\bar{1} = -1$ and $\bar{M} = -M$. This leads to the total effect on the light beam being expressed as

$$\begin{aligned} \hat{V}_+ &= \Omega_R \sum_{\varepsilon,m,M} \hat{e}_q \bar{1}^{F-M} \begin{pmatrix} F & 1 & f \\ \bar{M} & \varepsilon & m \end{pmatrix} |FM\rangle\langle fm|, \\ \hat{H}_e &\to \hat{H}_e - \hat{P}_e \hbar\omega, \end{aligned} \tag{A17}$$

and $\hat{V}_- = \hat{V}_+^\dagger$.

3. Generalized rotating-wave approximation

As mentioned in Sec. III, when the system involves several distinct time-dependent interactions, it is often more effective to apply a generalized form of the RWA rather than a sequence of standard RWAs. This generalized transformation can be implemented using the following unitary operation:

$$\hat{U}_{\rm grwa} = \exp(-i\hat{G}t), \tag{A18}$$

where $\hat{G}$ is a time-independent generator of the transformation. The choice of $\hat{G}$ is not unique; however, a reasonable approach is to identify the frequency differences between coupled states and construct $\hat{G}$ as a diagonal operator encoding these detunings. Importantly, applying a time-dependent basis transformation induces an effective energy shift determined by $\hat{G}$:

$$\hat{\tilde{H}} = \hat{U}_{\rm grwa}^\dagger \hat{H} \hat{U}_{\rm grwa} - i\hat{U}_{\rm grwa}^\dagger \frac{\partial}{\partial t} \hat{U}_{\rm grwa} = \hat{U}_{\rm grwa}^\dagger \hat{H} \hat{U}_{\rm grwa} - \hat{G}. \tag{A19}$$

This implies that $\hat{G}$ should be chosen to simplify the system's energy structure while minimizing the introduction of unnecessary scalar terms in the Hamiltonian. In our case, the simplest choice—yielding the desired form of the Hamiltonian, as outlined in Ref. [49]—reads

$$\hat{G} = \omega_{\rm RF} \hat{P}_g \hat{F}_z \hat{P}_g + \omega \hat{P}_e = \begin{pmatrix} \omega_{\rm RF} & 0 & 0 & 0 \\ 0 & 0 & 0 & 0 \\ 0 & 0 & -\omega_{\rm RF} & 0 \\ 0 & 0 & 0 & \omega \end{pmatrix}. \tag{A20}$$

This leads to the transformation

$$\begin{aligned} \hat{U}_{\rm grwa} &= \hat{P}_g e^{-i\omega_{\rm RF} \hat{F}_z t} + \hat{P}_e e^{-i\omega t} \\ &= \begin{pmatrix} e^{-i\omega_{\rm RF} t} & 0 & 0 & 0 \\ 0 & 1 & 0 & 0 \\ 0 & 0 & e^{i\omega_{\rm RF} t} & 0 \\ 0 & 0 & 0 & e^{-i\omega t} \end{pmatrix}. \end{aligned} \tag{A21}$$

Applying the above transformation and neglecting rapidly oscillating terms at frequencies $2\omega_{\rm RF}$ and 2ω, the explicit time dependence is eliminated from the Hamiltonian. This results in effective energy-level shifts described by the diagonal matrix: $\mathrm{diag}([-\omega_{\rm RF}, 0, \omega_{\rm RF}, -\omega])$.

4. Alternative forms of the master equation

It is important to note that different conventions exist for formulating the quantum master equation—also known as the quantum Liouville equation, also known as the Lindblad or Gorini-Kossakowski-Lindblad-Sudarshan equation. In the

context of this paper, two commonly used forms are particularly relevant: one prevalent in AMO physics and another widely adopted in quantum information and quantum optics.

The most commonly used form of the master equation in quantum optics is given in Eq. (1), where relaxation processes are described by a set of independent jump operators $\hat{L}_\mu$. This formulation is particularly convenient, as it allows for a comprehensive characterization of the system's dissipative dynamics and facilitates further simplifications using the effective operator or superoperator formalisms.

In contrast, an alternative yet equivalent form of the master equation is commonly employed in atomic physics:

$$\frac{\mathrm{d}\rho}{\mathrm{d}t} = \mathcal{L}(\rho) = -i[\hat{H}, \rho] - \frac{1}{2}\{\hat{\Gamma}, \rho\} + \hat{\Lambda}(\rho), \tag{A22}$$

where $\hat{\Gamma}$ and $\hat{\Lambda}(\rho)$ denote the relaxation and repopulation operators, respectively [49,55]. These operators are usually introduced phenomenologically, as they capture not only the internal dynamics of the atomic system but also external effects—such as atoms leaving the interaction region or being replenished by new atoms entering the system.

Although the two forms differ in appearance, they are mathematically equivalent under suitable identifications. Their structural similarities are readily apparent, enabling a direct correspondence between the jump-operator and relaxation-repopulation representations:

$$\hat{\Gamma} = \sum_\mu \hat{L}_\mu^\dagger \hat{L}_\mu, \tag{A23}$$

$$\hat{\Lambda}(\rho) = \sum_\mu \hat{L}_\mu \rho \hat{L}_\mu^\dagger. \tag{A24}$$

It is worth noting that although the transformation from jump operators to relaxation and repopulation terms is relatively straightforward, the inverse transformation is generally ambiguous and not uniquely defined.

APPENDIX B: SUPEROPERATOR FORMALISM

As discussed in Sec. I, calculating LEPs usually requires expressing the Liouvillian operator in a superoperator basis. For easier comparison, it is also beneficial to represent the NHH in the same basis. Since the choice of basis is not unique, there are multiple possible implementations. Two common approaches are vectorization into the Fock-Liouville space using right- and left-hand-side operators, and expansion in the generalized Gell-Mann basis [104].

1. Liouvillians in the generalized Gell-Mann basis

Here, we recall how the Liouvillian of a d-level system can be represented in the basis formed by the generalized Gell-Mann matrices, which are also commonly referred to as generalized Pauli matrices, particularly in the context of quantum information.

To begin, it is important to note that these matrices, together with the identity matrix—denoted as the set $\{\hat{\sigma}_i : i < d^2\}$, where $\hat{\sigma}_{d^2} \propto \hat{1}$—form a basis for real-valued expansions of Hermitian matrices [104]. Generally, such a basis can be constructed following the method outlined in Ref. [104], which reduces to the standard Pauli matrices for $d = 2$ and the standard Gell-Mann matrices for $d = 3$. This property makes the basis particularly well suited for standard Hermitian Hamiltonians.

For NHHs, however, an additional complication arises: Representing an arbitrary non-Hermitian $d \times d$ matrix requires extending the basis. This issue can be addressed by allowing the expansion coefficients to be complex.

Another crucial property of the generalized Gell-Mann matrices is that they satisfy the standard orthogonality relation, $\mathrm{Tr}(\hat{\sigma}_i\hat{\sigma}_j) = 2\delta_{ij}$. This property enables the straightforward vectorization of density matrices as follows:

$$\hat{\rho} = \sum_{i=1}^{d^2} \left[\frac{1}{2}\mathrm{Tr}(\rho\hat{\sigma}_i)\right]\hat{\sigma}_i = \sum_{i=1}^{d^2} \rho_i\hat{\sigma}_i = |\rho\rangle\!\rangle, \tag{B1}$$

where $|\rho\rangle\!\rangle$ represents the vectorized density matrix with elements $|\rho\rangle\!\rangle_i = \mathrm{Tr}(\rho\hat{\sigma}_i)/2$. The next step is to express the Liouvillian as a linear operator acting on this vectorized form:

$$\hat{\hat{\mathcal{L}}}_{ij} = \tfrac{1}{2}\mathrm{Tr}[\mathcal{L}(\hat{\sigma}_j)\hat{\sigma}_i]. \tag{B2}$$

To achieve this, Eq. (1) can be decomposed into three parts: the Hamiltonian component $\hat{\hat{H}}$, the non-Hermitian but coherent part $\hat{\hat{\Gamma}}$, and the quantum-jump term $\hat{\hat{\Lambda}}$. This separation naturally leads to the introduction of the NHH superoperator defined as $\hat{\hat{H}}_{\mathrm{NH}} = \hat{\hat{H}} + i\hat{\hat{\Gamma}}$:

$$\mathcal{L}(\rho) \to \hat{\hat{\mathcal{L}}}|\rho\rangle\!\rangle = (-i\hat{\hat{H}} + \hat{\hat{\Gamma}} + \hat{\hat{\Lambda}})|\rho\rangle\!\rangle = (-i\hat{\hat{H}}_{\mathrm{NH}} + \hat{\hat{\Lambda}})|\rho\rangle\!\rangle. \tag{B3}$$

The first term expands as

$$[\hat{H}, \rho] = \sum_{i=1}^{d^2} [\hat{H}, \hat{\sigma}_i]\rho_i = \sum_{i,j=1}^{d^2} \frac{1}{2}\mathrm{Tr}([\hat{H}, \hat{\sigma}_i]\hat{\sigma}_j)\rho_i\hat{\sigma}_j$$

$$= \sum_{i,j=1}^{d^2} \hat{\sigma}_j\hat{\hat{H}}_{ji}|\rho\rangle\!\rangle_i = \hat{\hat{H}}|\rho\rangle\!\rangle, \tag{B4}$$

where $\hat{\hat{H}}$ is a matrix with elements given by

$$\hat{\hat{H}}_{ij} = \tfrac{1}{2}\mathrm{Tr}([\hat{H}, \hat{\sigma}_j]\hat{\sigma}_i). \tag{B5}$$

Analogously, the second term in Eq. (1) expands as

$$-\frac{1}{2}\sum_\mu \{\hat{L}_\mu^\dagger\hat{L}_\mu, \rho\} = -\frac{1}{2}\sum_{i,j=1}^{d^2}\left[\frac{1}{2}\sum_\mu \mathrm{Tr}(\{\hat{L}_\mu^\dagger\hat{L}_\mu, \hat{\sigma}_i\}\hat{\sigma}_j)\right]\rho_i\hat{\sigma}_j$$

$$= \sum_{i,j=1}^{d^2} \hat{\sigma}_j\hat{\hat{\Gamma}}_{ji}|\rho\rangle\!\rangle_i = \hat{\hat{\Gamma}}|\rho\rangle\!\rangle, \tag{B6}$$

where $\hat{\hat{\Gamma}}$ is given by

$$\hat{\hat{\Gamma}}_{ij} = -\frac{1}{4}\sum_\mu \mathrm{Tr}(\{\hat{L}_\mu^\dagger\hat{L}_\mu, \hat{\sigma}_j\}\hat{\sigma}_i). \tag{B7}$$

The last term, describing quantum jumps, reads

$$\sum_{\mu}\hat{L}_{\mu}^{\dagger}\rho\hat{L}_{\mu}=\sum_{i,j=1}^{d^2}\frac{1}{2}\sum_{\mu}\mathrm{Tr}(\hat{L}_{\mu}^{\dagger}\hat{\sigma}_i\hat{L}_{\mu}\hat{\sigma}_j)\rho_i\hat{\sigma}_j$$
$$=\sum_{i,j=1}^{d^2}\hat{\sigma}_j\hat{\hat{\Lambda}}_{ji}|\rho\rangle\rangle_i=\hat{\hat{\Lambda}}|\rho\rangle\rangle, \tag{B8}$$

where $\hat{\hat{\Lambda}}$ is given by

$$\hat{\hat{\Lambda}}_{ij}=\frac{1}{2}\sum_{\mu}\mathrm{Tr}(\hat{L}_{\mu}^{\dagger}\hat{\sigma}_j\hat{L}_{\mu}\hat{\sigma}_i). \tag{B9}$$

2. Liouvillians in the Liouville-Fock basis

Expanding a Liouvillian of d-level system in the generalized Gell-Mann basis is a natural choice, especially from the perspective of experimentally implemented process tomography. However, this approach can initially seem counterintuitive when the system of interest is not simply a single-spin system—for example, a two-level system where the excited state is explicitly retained rather than eliminated. Despite this, such impressions are generally misleading, as the generalized Gell-Mann basis can represent any finite-dimensional system.

Alternatively, this opens the door to a different approach based on expansion in the Liouville-Fock basis. This method inherently vectorizes the density matrix [62], transforming it as follows:

$$\rho=\sum_{i,j}\rho_{ij}|i\rangle\langle j|\longrightarrow|\rho\rangle\rangle=\sum_{i,j}\rho_{ij}|i\rangle\otimes|j^*\rangle. \tag{B10}$$

In this formalism, the density matrix is transformed into a vector by sequentially stacking its elements column by column.

To complete the framework, it is necessary to define the right-hand-side and left-hand-side acting superoperators, denoted as $\hat{\hat{R}}[\hat{\Gamma}]$ and $\hat{\hat{L}}[\hat{\Gamma}]$, respectively. These superoperators can be expressed as

$$\hat{\hat{L}}[\hat{\Gamma}]|\rho\rangle\rangle=(\hat{\Gamma}\otimes\hat{1})|\rho\rangle\rangle=\sum_{i,j}\rho_{ij}(\hat{\Gamma}|i\rangle)\otimes|j^*\rangle$$
$$\longrightarrow\sum_{i,j}\rho_{ij}\hat{\Gamma}|i\rangle\langle j|=\hat{\Gamma}\rho,$$
$$\hat{\hat{R}}[\hat{\Gamma}]|\rho\rangle\rangle=(\hat{1}\otimes\hat{\Gamma}^T)|\rho\rangle\rangle\longrightarrow\rho\hat{\Gamma}. \tag{B11}$$

By adopting this convention, the Liouvillian (1) in the master equation can be expressed as

$$\hat{\hat{\mathcal{L}}}=-i(\hat{H}\otimes\hat{1}-\hat{1}\otimes\hat{H}^T)$$
$$+\sum_{\mu}\left[\hat{L}_{\mu}\otimes\hat{L}_{\mu}^*-\frac{1}{2}(\hat{L}_{\mu}^{\dagger}\hat{L}_{\mu}\otimes\hat{1}+\hat{1}\otimes\hat{L}_{\mu}^T\hat{L}_{\mu}^*)\right]. \tag{B12}$$

3. Properties of the Hamiltonian superoperator

Following the definition of the superoperator $\hat{\hat{H}}_{ij}$ in Eq. (B5), we establish two key properties: It is represented by an antisymmetric and purely imaginary matrix.

First, we demonstrate the antisymmetry property:

$$\hat{\hat{H}}_{ij}=\tfrac{1}{2}\mathrm{Tr}([\hat{H},\hat{\sigma}_j]\hat{\sigma}_i)$$
$$=\tfrac{1}{2}\{\mathrm{Tr}(\hat{H}\hat{\sigma}_j\hat{\sigma}_i)-\mathrm{Tr}(\hat{\sigma}_j\hat{H}\hat{\sigma}_i)\}$$
$$=\tfrac{1}{2}\{\mathrm{Tr}(\hat{H}\hat{\sigma}_j\hat{\sigma}_i)-\mathrm{Tr}(\hat{H}\hat{\sigma}_i\hat{\sigma}_j)\}=-\hat{\hat{H}}_{ji}. \tag{B13}$$

This shows that $\hat{\hat{H}}$ is antisymmetric. Importantly, this result relies only on the cyclic property of the trace and thus holds regardless of the chosen basis.

Next, we demonstrate that the elements $\hat{\hat{H}}_{ij}$ are purely imaginary by computing the complex conjugate of its matrix elements:

$$(\hat{\hat{H}}_{ij})^*=\tfrac{1}{2}\mathrm{Tr}([\hat{H},\hat{\sigma}_j]\hat{\sigma}_i)^*$$
$$=\tfrac{1}{2}\mathrm{Tr}(\{[\hat{H},\hat{\sigma}_j]\hat{\sigma}_i\}^{\dagger})$$
$$=\tfrac{1}{2}\mathrm{Tr}(\hat{\sigma}_i^{\dagger}[\hat{H},\hat{\sigma}_j]^{\dagger}). \tag{B14}$$

Since both $\hat{\sigma}_i$ and $\hat{H}$ are Hermitian, we can use the property

$$[\hat{H},\hat{\sigma}_i]^{\dagger}=(\hat{H}\hat{\sigma}_i-\hat{\sigma}_i\hat{H})^{\dagger}=\hat{\sigma}_i^{\dagger}\hat{H}^{\dagger}-\hat{H}^{\dagger}\hat{\sigma}_i^{\dagger}=[\hat{\sigma}_i,\hat{H}]. \tag{B15}$$

Substituting this into our previous expression and applying the cyclic property of the trace, we obtain

$$\hat{\hat{H}}_{ij}^*=\tfrac{1}{2}\mathrm{Tr}(\hat{\sigma}_i^{\dagger}[\hat{H},\hat{\sigma}_j]^{\dagger})=\tfrac{1}{2}\mathrm{Tr}(\hat{\sigma}_i[\hat{\sigma}_j,\hat{H}])$$
$$=\mathrm{Tr}([\hat{\sigma}_j,\hat{H}]\hat{\sigma}_i)=-\mathrm{Tr}([\hat{H},\hat{\sigma}_j]\hat{\sigma}_i)=-\hat{\hat{H}}_{ij}. \tag{B16}$$

This confirms that $\hat{\hat{H}}_{ij}$ is purely imaginary.

4. Properties of the non-Hermitian coherent part in Liouvillians

Analogously, we now establish the key properties of the superoperator $\hat{\hat{\Gamma}}_{ij}$ defined in Eq. (B7). In particular, we show that it is symmetric and real-valued.

The symmetry property follows by an argument similar to the antisymmetry of $\hat{\hat{H}}$:

$$\hat{\hat{\Gamma}}_{ij}=-\tfrac{1}{4}\mathrm{Tr}(\{\hat{\Gamma},\hat{\sigma}_j\}\hat{\sigma}_i)$$
$$=-\tfrac{1}{4}[\mathrm{Tr}(\hat{\Gamma}\hat{\sigma}_j\hat{\sigma}_i)+\mathrm{Tr}(\hat{\sigma}_j\hat{\Gamma}\hat{\sigma}_i)]$$
$$=-\tfrac{1}{4}[\mathrm{Tr}(\hat{\Gamma}\hat{\sigma}_j\hat{\sigma}_i)+\mathrm{Tr}(\hat{\Gamma}\hat{\sigma}_i\hat{\sigma}_j)]=\hat{\hat{\Gamma}}_{ji}. \tag{B17}$$

This confirms that $\hat{\hat{\Gamma}}$ is a symmetric matrix.

To demonstrate that $\hat{\hat{\Gamma}}$ is real-valued, we first note that although the jump operators $\hat{L}_{\mu}$ may be non-Hermitian, the operator $\hat{\Gamma}=\hat{L}_{\mu}^{\dagger}\hat{L}_{\mu}$ is always Hermitian. This observation allows us to write

$$\{\hat{\Gamma},\hat{\sigma}_i\}^{\dagger}=\{\hat{\Gamma}^{\dagger},\hat{\sigma}_i^{\dagger}\}=\{\hat{\Gamma},\hat{\sigma}_i\}. \tag{B18}$$

Using similar reasoning as in the previous case, we compute the complex conjugate:

$$\hat{\hat{\Gamma}}_{ij}^*=-\tfrac{1}{4}\mathrm{Tr}(\{\hat{\Gamma},\hat{\sigma}_j\}\hat{\sigma}_i)^*=-\tfrac{1}{4}\mathrm{Tr}(\hat{\sigma}_i^{\dagger}\{\hat{\Gamma},\hat{\sigma}_j\}^{\dagger})$$
$$=-\tfrac{1}{4}\mathrm{Tr}(\hat{\sigma}_i\{\hat{\Gamma},\hat{\sigma}_j\})=\mathrm{Tr}(\{\hat{\Gamma},\hat{\sigma}_j\}\hat{\sigma}_i)=\hat{\hat{\Gamma}}_{ij}. \tag{B19}$$

This confirms that $\hat{\hat{\Gamma}}$ is a real-valued matrix.

5. Correspondence between operator and superoperator spectra

It is straightforward to observe that a superoperator, represented by a $d^2 \times d^2$ matrix, has d^2 eigenvalues, whereas the underlying Hamiltonian operator from which it is derived possesses only d eigenvalues. This discrepancy implies that the superoperator spectrum must exhibit a degree of redundancy or degeneracy, as it cannot encode more information than the original operator's spectrum. Consequently, one expects a direct and structured relationship between the spectra of the operator and its associated superoperator.

To investigate this relationship, we first observe that for any linear operator, the right and left eigenvalue problems yield identical eigenvalues, even though the corresponding eigenvectors are generally distinct. This equivalence arises because both formulations are governed by the same characteristic equation:

$$\hat{H}_{\rm NH}|u\rangle = E|u\rangle, \quad \langle v|\hat{H}_{\rm NH} = E\langle v|,$$
$$(\hat{H}_{\rm NH} - \hat{1}E)|u\rangle = 0, \quad \langle v|(\hat{H}_{\rm NH} - \hat{1}E) = 0. \tag{B20}$$

Thus, the characteristic equation in both cases takes the form

$$\det(\hat{H}_{\rm NH} - \hat{1}E) = 0. \tag{B21}$$

To analyze the eigenvalue problem of the corresponding superoperator $\hat{\hat{H}}_{\rm NH}$, we proceed as follows:

$$\hat{\hat{H}}_{\rm NH}|\lambda\rangle\!\rangle = \lambda|\lambda\rangle\!\rangle \Rightarrow \hat{H}_{\rm NH}\hat{X} - \hat{X}\hat{H}_{\rm NH}^{\dagger} = \lambda\hat{X}, \tag{B22}$$

where the superoperator is expressed in operator form, as given in Eq. (3), and X denotes the operator whose vectorized form is $|\lambda\rangle\!\rangle$ [see, e.g., Eq. (B1) or (B10)].

Since $\hat{X}$ must be preserved under the action of $\hat{H}_{\rm NH}$ from both the left and the right, it is natural to construct $\hat{X}$ from the right and left eigenvectors of $\hat{H}_{\rm NH}$, such that $\hat{X}_{ij} = |u_i\rangle\langle v_j|$. Substituting this form into the eigenvalue equation yields

$$\begin{aligned}\hat{\hat{H}}_{\rm NH}|\lambda_{ij}\rangle\!\rangle &= \hat{H}_{\rm NH}\hat{X}_{ij} - \hat{X}_{ij}\hat{H}_{\rm NH}^{\dagger} \\ &= \hat{H}_{\rm NH}|u_i\rangle\langle v_j| - |u_i\rangle\langle v_j|\hat{H}_{\rm NH}^{\dagger} \\ &= (E_i - E_j^*)|u_i\rangle\langle v_j|. \end{aligned}\tag{B23}$$

This derivation demonstrates that the spectrum of the non-Hermitian superoperator $\hat{\hat{H}}_{\rm NH}$ is fully determined by the eigenvalues of the underlying operator $\hat{H}_{\rm NH}$. However, the superoperator spectrum is not merely a subset of the operator spectrum; instead, it exhibits a richer structure formed from all possible pairwise differences between the operator's eigenvalues and their complex conjugates.

The structure of Eq. (B23) reveals that spectral degeneracies in the NHH operator, i.e., when $E_i = E_j$, directly translate into degeneracies in the corresponding superoperator spectrum. Specifically, the eigenvalues $\lambda_{ii} = \lambda_{ij} = \lambda_{ji} = \lambda_{jj} = 2\,\mathrm{Im}(E_i)$ become degenerate.

This observation can be generalized: An n-fold degeneracy in the spectrum of an NHH operator induces at least an n^2-fold degeneracy in the spectrum of the corresponding superoperator. It is important to emphasize that this represents only a lower bound on the degeneracy order in the superoperator spectrum—additional degeneracies may emerge depending on the specific structure of the operator and the relationships between its left and right eigenvectors.

APPENDIX C: ADDITIONAL ISOTROPIC RELAXATION IN THE SUPEROPERATOR DESCRIPTION

Following the approach outlined in Sec. IV B, we incorporate isotropic relaxation within the superoperator framework. To enable a direct comparison with the results obtained for LEPs, we introduce the following modified form of the hybrid Liouvillian:

$$\hat{\hat{\mathcal{L}}}_g(q) = \hat{\hat{\mathcal{L}}}(q) + \hat{\hat{\Gamma}}_{\rm g} + q\hat{\hat{\Lambda}}_{\rm g}, \tag{C1}$$

where $\hat{\hat{\mathcal{L}}}(q)$ is the hybrid Liouvillian defined in Eq. (27). The operators $\hat{\hat{\Gamma}}_g$ and $\hat{\hat{\Lambda}}_g$ represent, respectively, the hyperfine relaxation and repopulation (quantum jump) contributions in the superoperator basis. As a result, the matrix representation of the modified hybrid Liouvillian becomes

$$\begin{aligned}&\hat{\hat{\mathcal{L}}}_g(q) \\ &= \hat{\hat{\mathcal{L}}}(q) - \gamma \begin{pmatrix} 1 & 0 & 0 & 0 & 0 & 0 & 0 & 0 & 0 \\ 0 & 1 & 0 & 0 & 0 & 0 & 0 & 0 & 0 \\ 0 & 0 & 1 & 0 & 0 & 0 & 0 & 0 & 0 \\ 0 & 0 & 0 & 1 & 0 & 0 & 0 & 0 & 0 \\ 0 & 0 & 0 & 0 & 1 & 0 & 0 & 0 & 0 \\ 0 & 0 & 0 & 0 & 0 & 1 & 0 & 0 & 0 \\ 0 & 0 & 0 & 0 & 0 & 0 & 1 & 0 & 0 \\ 0 & 0 & 0 & 0 & 0 & 0 & 0 & 1 & 0 \\ 0 & 0 & 0 & 0 & 0 & 0 & 0 & 0 & 1-q \end{pmatrix}. \end{aligned}\tag{C2}$$

In general, this modification substantially affects the superoperator spectrum. However, in the limiting cases of $q = 0$ (corresponding to the NHH limit) and $q = 1$ (representing the pure Liouvillian case), the resulting spectral changes are notably simple and analytically tractable.

For the pure NHH limit ($q = 0$), the original spectrum [see Eq. (31)] is modified to

$$\begin{aligned}&\{-\gamma, -2\Omega - \gamma, -\alpha_1^* - \gamma, -\alpha_1^* - \gamma, -\alpha_1 - \gamma, \\ &\quad -\alpha_1 - \gamma, -2\alpha_1 - \gamma, -2\alpha_1^* - \gamma, -2\Omega - \gamma\}, \end{aligned}\tag{C3}$$

which corresponds to a uniform shift of the real part of the spectrum by $-\gamma$. This aligns with the nature of isotropic relaxation, which imposes uniform damping on all eigenmodes.

Similarly, in the $q = 1$ case (the fully trace-preserving Liouvillian regime), all eigenvalues are uniformly shifted by $-\gamma$, with the exception of the stationary state at $\lambda = 0$. This behavior highlights the isotropic nature of the relaxation process while ensuring the trace preservation of the density matrix.

[1] T. Kato, *Perturbation Theory for Linear Operators* (Springer, New York, 1966).

[2] W. D. Heiss, Repulsion of resonance states and exceptional points, Phys. Rev. E **61**, 929 (2000).

[3] C. Dembowski, H.-D. Graf, H. L. Harney, A. Heine, W. D. Heiss, H. Rehfeld, and A. Richter, Experimental observation of the topological structure of exceptional points, Phys. Rev. Lett. **86**, 787 (2001).

[4] M. V. Berry, Physics of non-Hermitian degeneracies, Czech. J. Phys. **54**, 1039 (2004).

[5] C. M. Bender and S. Boettcher, Real spectra in non-Hermitian Hamiltonians having $\mathcal{PT}$ symmetry, Phys. Rev. Lett. **80**, 5243 (1998).

[6] C. M. Bender, Making sense of non-Hermitian Hamiltonians, Rep. Prog. Phys. **70**, 947 (2007).

[7] W. D. Heiss, The physics of exceptional points, J. Phys. A: Math. Theor. **45**, 444016 (2012).

[8] Ş. K. Özdemir, S. Rotter, F. Nori, and L. Yang, Parity-time symmetry and exceptional points in photonics, Nat. Mater. **18**, 783 (2019).

[9] M. Miri and A. Alù, Exceptional points in optics and photonics, Science **363**, eaar7709 (2019).

[10] M. Parto, Y. G. N. Liu, B. Bahari, M. Khajavikhan, and D. N. Christodoulides, Non-Hermitian and topological photonics: Optics at an exceptional point, Nanophotonics **10**, 403 (2021).

[11] A. Guo, G. J. Salamo, D. Duchesne, R. Morandotti, M. Volatier-Ravat, V. Aimez, G. A. Siviloglou, and D. N. Christodoulides, Observation of $\mathcal{PT}$-symmetry breaking in complex optical potentials, Phys. Rev. Lett. **103**, 093902 (2009).

[12] C. Rüter, K. Makris, R. El-Ganainy, D. N. Christodoulides, M. Segev, and D. Kip, Observation of parity-time symmetry in optics, Nat. Phys. **6**, 192 (2010).

[13] A. Regensburger, C. Bersch, M.-A. Miri, G. Onishchukov, D. N. Christodoulides, and U. Peschel, Parity-time synthetic photonic lattices, Nature (London) **488**, 167 (2012).

[14] B. Zhen *et al.*, Spawning rings of exceptional points out of Dirac cones, Nature (London) **525**, 354 (2015).

[15] K. Ding, Z. Q. Zhang, and C. T. Chan, Coalescence of exceptional points and phase diagrams for one-dimensional $\mathcal{PT}$-symmetric photonic crystals, Phys. Rev. B **92**, 235310 (2015).

[16] A. Cerjan, A. Raman, and S. Fan, Exceptional contours and band structure design in parity-time symmetric photonic crystals, Phys. Rev. Lett. **116**, 203902 (2016).

[17] L. Feng, R. El-Ganainy, and L. Ge, Non-Hermitian photonics based on parity-time symmetry, Nat. Photon. **11**, 752 (2017).

[18] R. El-Ganainy, M. Khajavikhan, D. N. Christodoulides, and Ş. K. Özdemir, The dawn of non-Hermitian optics, Commun. Phys. **2**, 37 (2019).

[19] J. Schindler, A. Li, M. C. Zheng, F. M. Ellis, and T. Kottos, Experimental study of active LRC circuits with $\mathcal{PT}$ symmetries, Phys. Rev. A **84**, 040101(R) (2011).

[20] H. Benisty *et al.*, Implementation of $\mathcal{PT}$ symmetric devices using plasmonics: Principle and applications, Opt. Express **19**, 18004 (2011).

[21] H. Alaeian and J. A. Dionne, Parity-time-symmetric plasmonic metamaterials, Phys. Rev. A **89**, 033829 (2014).

[22] P.-C. Kuo, N. Lambert, A. Miranowicz, G.-Y. Chen, Y.-N. Chen, and F. Nori, Collectively induced exceptional points of quantum emitters coupled to nanoparticle surface plasmons, Phys. Rev. A **101**, 013814 (2020).

[23] X. Zhu, H. Ramezani, C. Shi, J. Zhu, and X. Zhang, $\mathcal{PT}$-symmetric acoustics, Phys. Rev. X **4**, 031042 (2014).

[24] H. Jing, Ş. K. Özdemir, X.-Y. Lu, J. Zhang, L. Yang, and F. Nori, $\mathcal{PT}$-symmetric phonon laser, Phys. Rev. Lett. **113**, 053604 (2014).

[25] R. Fleury, D. L. Sounas, and A. Alu, An invisible acoustic sensor based on parity-time symmetry, Nat. Commun. **6**, 5905 (2015).

[26] K. Ding, G. Ma, M. Xiao, Z. Q. Zhang, and C. T. Chan, Emergence, coalescence, and topological properties of multiple exceptional points and their experimental realization, Phys. Rev. X **6**, 021007 (2016).

[27] H. Lü, Ş. K. Özdemir, L. M. Kuang, F. Nori, and H. Jing, Exceptional points in random-defect phonon lasers, Phys. Rev. Appl. **8**, 044020 (2017).

[28] J. Zhang *et al.*, A phonon laser operating at an exceptional point, Nat. Photon. **12**, 479 (2018).

[29] H. Jing *et al.*, Optomechanically-induced transparency in parity-timesymmetric microresonators, Sci. Rep. **5**, 9663 (2015).

[30] D. W. Schönleber, A. Eisfeld, and R. El-Ganainy, Optomechanical interactions in non-Hermitian photonic molecules, New J. Phys. **18**, 045014 (2016).

[31] H. Xu, D. Mason, L. Jiang, and J. G. E. Harris, Topological energy transfer in an optomechanical system with exceptional points, Nature (London) **537**, 80 (2016).

[32] H. Jing, Ş. K. Özdemir, H. Lü, and F. Nori, High-order exceptional points in optomechanics, Sci. Rep. **7**, 3386 (2017).

[33] Z. Zhang *et al.*, Observation of parity-time symmetry in optically induced atomic lattices, Phys. Rev. Lett. **117**, 123601 (2016).

[34] M. Naghiloo, M. Abbasi, Y. N. Joglekar, and K. W. Murch, Quantum state tomography across the exceptional point in a single dissipative qubit, Nat. Phys. **15**, 1232 (2019).

[35] W. Chen, M. Abbasi, Y. N. Joglekar, and K. W. Murch, Quantum jumps in the non-Hermitian dynamics of a superconducting qubit, Phys. Rev. Lett. **127**, 140504 (2021).

[36] W. Chen, M. Abbasi, B. Ha, S. Erdamar, Y. N. Joglekar, K. W. Murch, Decoherence induced exceptional points in a dissipative superconducting qubit, Phys. Rev. Lett. **128**, 110402 (2022).

[37] A. Roy, S. Jahani, Q. Guo, A. Dutt, S. Fan, M.-A. Miri, and A. Marandi, Nondissipative non-Hermitian dynamics and exceptional points in coupled optical parametric oscillators, Optica **8**, 415 (2021).

[38] A. Roy, S. Jahani, C. Langrock, M. Fejer, and A. Marandi, Spectral phase transitions in optical parametric oscillators, Nat. Commun. **12**, 835 (2021).

[39] S. Jahani, A. Roy, and A. Marandi, Wavelength-scale optical parametric oscillators, Optica **8**, 262 (2021).

[40] M. Sheikhey, A. Fard, and H. Baghban, Non-Hermitian gauged topological laser with multi protected modes, Phys. Scr. **96**, 125829 (2021).

[41] M. Kang, F. Liu, and J. Li, Effective spontaneous $\mathcal{PT}$-symmetry breaking in hybridized metamaterials, Phys. Rev. A **87**, 053824 (2013).

[42] R. Fleury, D. L. Sounas, and A. Alo, Negative refraction and planar focusing based on parity-time symmetric metasurfaces, Phys. Rev. Lett. **113**, 023903 (2014).

[43] Y. Sun, W. Tan, H.-Q. Li, J. Li, and H. Chen, Experimental demonstration of a coherent perfect absorber with $\mathcal{PT}$ phase transition, Phys. Rev. Lett. **112**, 143903 (2014).
[44] M. Kang, J. Chen, and Y. D. Chong, Chiral exceptional points in metasurfaces, Phys. Rev. A **94**, 033834 (2016).
[45] S. Xiao, J. Gear, S. Rotter, and J. Li, Effective $\mathcal{PT}$-symmetric metasurfaces for subwavelength amplified sensing, New J. Phys. **18**, 085004 (2016).
[46] T. Gao *et al.*, Observation of non-Hermitian degeneracies in a chaotic exciton-polariton billiard, Nature (London) **526**, 554 (2015).
[47] P. Peng *et al.*, Anti-parity-time symmetry with flying atoms, Nat. Phys. **12**, 1139 (2016).
[48] L. Ding, K. Shi, Q. Zhang, D. Shen, X. Zhang, and W. Zhang, Experimental determination of $\mathcal{PT}$-symmetric exceptional points in a single trapped ion, Phys. Rev. Lett. **126**, 083604 (2021).
[49] C. Liang, Y. Tang, A.-N. Xu, and Y.-C. Liu, Observation of exceptional points in thermal atomic ensembles, Phys. Rev. Lett. **130**, 263601 (2023).
[50] J. L. Miller, Exceptional points make for exceptional sensors, Phys. Today **70**(10), 23 (2017).
[51] J. Wiersig, Review of exceptional point-based sensors, Photon. Res. **8**, 1457 (2020).
[52] J. Wiersig, Prospects and fundamental limits in exceptional point-based sensing, Nat. Commun. **11**, 2454 (2020).
[53] N. Hatano, Exceptional points of the Lindblad operator of a two-level system, Mol. Phys. **117**, 2121 (2019).
[54] F. Minganti, A. Miranowicz, R. Chhajlany, and F. Nori, Quantum exceptional points of non-Hermitian Hamiltonians and Liouvillians: The effects of quantum jumps, Phys. Rev. A **100**, 062131 (2019).
[55] M. Auzinsh, D. Budker, and S. M. Rochester, *Optically Polarized Atoms: Understanding Light-Atom Interactions* (Oxford University Press, Oxford, 2010).
[56] F. Minganti, A. Miranowicz, R. W. Chhajlany, I. I. Arkhipov, and F. Nori, Hybrid-Liouvillian formalism connecting exceptional points of non-Hermitian Hamiltonians and Liouvillians via postselection of quantum trajectories, Phys. Rev. A **101**, 062112 (2020).
[57] C.-Y. Ju, A. Miranowicz, G.-Y. Chen, F. Nori, Non-Hermitian Hamiltonians and no-go theorems in quantum information, Phys. Rev. A **100**, 062118 (2019).
[58] C.-Y. Ju, A. Miranowicz, F. Minganti, C.-T. Chan, G.-Y. Chen, and F. Nori, Flattening the curve with Einstein's quantum elevator: Hermitization of non-Hermitian Hamiltonians via the vielbein formalism, Phys. Rev. Res. **4**, 023070 (2022).
[59] C.-Y. Ju, A. Miranowicz, Y.-N. Chen, G.-Y. Chen, and F. Nori, Emergent parallel transports and curvatures in non-Hermitian quantum mechanics, Quantum **8**, 1277 (2024).
[60] C.-Y. Ju, A. Miranowicz, J. Barnett, G.-Y. Chen, and F. Nori, Heisenberg and Heisenberg-like representations via hilbert space bundle geometry in the non-Hermitian regime, Phys. Rev. A **111**, 052213 (2025).
[61] S. Erdamar, M. Abbasi, B. Ha, W. Chen, J. Muldoon, Y. Joglekar, and K. W. Murch, Constraining work fluctuations of non-Hermitian dynamics across the exceptional point of a superconducting qubit, Phys. Rev. Res. **6**, L022013 (2024).
[62] S. Abo, P. Tulewicz, K. Bartkiewicz, S. K. Özdemir, and A. Miranowicz, Experimental Liouvillian exceptional points in a quantum system without Hamiltonian singularities, New J. Phys. **26**, 123032 (2024).
[63] J.-W. Zhang *et al.*, Dynamical control of quantum heat engines using exceptional points, Nat. Commun. **13**, 6225 (2022).
[64] J.-T. Bu *et al.*, Enhancement of quantum heat engine by encircling a liouvillian exceptional point, Phys. Rev. Lett. **130**, 110402 (2023).
[65] J.-T. Bu *et al.*, Chiral quantum heating and cooling with an optically controlled ion, Light Sci. Appl. **13**, 143 (2024).
[66] S. Khandelwal, N. Brunner, and G. Haack, Signatures of liouvillian exceptional points in a quantum thermal machine, PRX Quantum **2**, 040346 (2021).
[67] J.-D. Lin, P.-C. Kuo, N. Lambert, A. Miranowicz, F. Nori, and Y.-N. Chen, Non-Markovian quantum exceptional points, Nat. Commun. **16**, 1289 (2025).
[68] M. V. Berry and M. Wilkinson, Diabolical points in the spectra of triangles, Proc. R. Soc. London A **392**, 15 (1984).
[69] I. I. Arkhipov, A. Miranowicz, F. Minganti, S. K. Özdemir, and F. Nori, Dynamically encircling an exceptional curve by crossing diabolic points: A programmable multimode switch, Nat. Commun. **14**, 2076 (2023).
[70] J. Naikoo, R. W. Chhajlany, and A. Miranowicz, Enhanced quantum sensing with hybrid exceptional-diabolic singularities, New J. Phys. **27**, 064505 (2025).
[71] J. Perina Jr., A. Miranowicz, G. Chimczak, and A. Kowalewska-Kudlaszyk, Quantum Liouvillian exceptional and diabolical points for bosonic fields with quadratic Hamiltonians: The Heisenberg-Langevin equation approach, Quantum **6**, 883 (2022).
[72] J. Peřina, A. Miranowicz, J. K. Kalaga, and W. Leoński, Unavoidability of nonclassicality loss in $\mathcal{PT}$-symmetric systems, Phys. Rev. A **108**, 033512 (2023).
[73] K. Thapliyal, J. Peřina Jr., G. Chimczak, A. Kowalewska-Kudłaszyk, and A. Miranowicz, Multiple quantum exceptional, diabolical, and hybrid points in multimode bosonic systems: I. Inherited and genuine singularities, arXiv:2405.01666.
[74] J. Peřina Jr., K. Thapliyal, G. Chimczak, A. Kowalewska-Kudłaszyk, and A. Miranowicz, Multiple quantum exceptional, diabolical, and hybrid points in multimode bosonic systems: II. Nonconventional $\mathcal{PT}$-symmetric dynamics and unidirectional coupling, arXiv:2405.01667.
[75] M. Anderson, J. Ensher, M. Matthews, C. Wieman, and E. A. Cornell, Observation of Bose-Einstein condensation in a dilute atomic vapor, Science **269**, 198 (1995).
[76] K. Davis, M. Mewes, M. Andrews, N. J. van Druten, D. S. Durfee, D. M. Kurn, and W. Ketterle, Bose-Einstein condensation in a gas of sodium atoms, Phys. Rev. Lett. **75**, 3969 (1995).
[77] M. Greiner, O. Mandel, T. Esslinger, T. W. Hänsch, and I. Bloch, Quantum phase transition from a superfluid to a Mott insulator in a gas of ultracold atoms, Nature (London) **415**, 39 (2002).
[78] P. S. Jessen and I. H. Deutsch, Optical lattices, in *Advances in Atomic, Molecular, and Optical Physics*, edited by B. Bederson and H. Walther (Academic Press, San Diego, CA, 1996), Vol. 37, pp. 95–138.
[79] W. Happer and A. Tam, Effect of rapid spin exchange on the magnetic-resonance spectrum of alkali vapors, Phys. Rev. A **16**, 1877 (1977).

[80] K. Mouloudakis, J. Kong, A. Sierant, E. Arkin, M. Hernndez Ruiz, R. Jiménez-Martinez, and M. Mitchell, Anomalous noise spectra in a spin-exchange-relaxation-free alkali-metal vapor, Phys. Rev. A **109**, L040802 (2024).

[81] J. Kong, R. Jiménez-Martinez, C. Troullinou, V. Lucivero, G. Tóth, and M. Mitchell, Measurement-induced, spatially-extended entanglement in a hot, strongly-interacting atomic system, Nat. Commun. **11**, 2415 (2020).

[82] M. V. Balabas, T. Karaulanov, M. P. Ledbetter, and D. Budker, Polarized alkali-metal vapor with minute-long transverse spin-relaxation time, Phys. Rev. Lett. **105**, 070801 (2010).

[83] O. Schmidt, R. Wynands, Z. Hussein, and D. Meschede, Steep dispersion and group velocity below *c*/3000 in coherent population trapping, Phys. Rev. A **53**, R27 (1996).

[84] K. Hammerer, K. Mölmer, E. Polzik, and J. Cirac, Light-matter quantum interface, Phys. Rev. A **70**, 044304 (2004).

[85] O. Katz, R. Shaham, E. Polzik, and O. Firstenberg, Long-lived entanglement generation of nuclear spins using coherent light, Phys. Rev. Lett. **124**, 043602 (2020).

[86] K. Jensen, W. Wasilewski, H. Krauter, T. Fernholz, B. Nielsen, M. Owari, M. Plenio, A. Serafini, M. Wolf, and E. Polzik, Quantum memory for entangled continuous-variable states, Nat. Phys. **7**, 13 (2011).

[87] E. Mikhailov and I. Novikova, Low-frequency vacuum squeezing via polarization self-rotation in Rb vapor, Opt. Lett. **33**, 1213 (2008).

[88] H. Dang, A. Maloof, and M. Romalis, Ultrahigh sensitivity magnetic field and magnetization measurements with an atomic magnetometer, Appl. Phys. Lett. **97**, 151110 (2010).

[89] W. Chalupczak, R. Godun, S. Pustelny, and W. Gawlik, Room temperature femtotesla radio-frequency atomic magnetometer, Appl. Phys. Lett. **100**, 242401 (2012).

[90] D. Budker and M. Romalis, Optical magnetometry, Nat. Phys. **3**, 227 (2007).

[91] T. Kornack, R. Ghosh, and M. Romalis, Nuclear spin gyroscope based on an atomic comagnetometer, Phys. Rev. Lett. **95**, 230801 (2005).

[92] S. Afach *et al.*, Search for topological defect dark matter with a global network of optical magnetometers, Nat. Phys. **17**, 1396 (2021).

[93] M. Padniuk, M. Kopciuch, R. Cipolletti, A. Wickenbrock, D. Budker, and S. Pustelny, Response of atomic spin-based sensors to magnetic and nonmagnetic perturbations, Sci. Rep. **12**, 324 (2022).

[94] F. Reiter and A. S. Sorensen, Effective operator formalism for open quantum systems, Phys. Rev. A **85**, 032111 (2012).

[95] B. Baumgartner and H. Narnhofer, Analysis of quantum semigroups with GKS-Lindblad generators: II. General, J. Phys. A: Math. Theor. **41**, 395303 (2008).

[96] V. V. Albert and L. Jiang, Symmetries and conserved quantities in Lindblad master equations, Phys. Rev. A **89**, 022118 (2014).

[97] P. Kumar, K. Snizhko, and Y. Gefen, Near-unit efficiency of chiral state conversion via hybrid-Liouvillian dynamics, Phys. Rev. A **104**, L050405 (2021).

[98] M. Kopciuch and S. Pustelny, Optical reconstruction of the collective density matrix of a qutrit, Phys. Rev. A **106**, 022406 (2022).

[99] M. Kopciuch, M. Smolis, A. Miranowicz, and S. Pustelny, Optimized experimental optical tomography of quantum states of room-temperature alkali-metal vapor, Phys. Rev. A **109**, 032402 (2024).

[100] R. T. Thew, K. Nemoto, A. G. White, and W. J. Munro, Qudit quantum state tomography, Phys. Rev. A **66**, 012303 (2002).

[101] G. O. Samach *et al.*, Lindblad tomography of a superconducting quantum processor, Phys. Rev. Appl. **18**, 064056 (2022).

[102] Y. Sun, M. Kopciuch, A. D. Fard, and S. Pustelny, Quantum process tomography of atomic vapors (unpublished).

[103] A. Messiah, *Quantum Mechanics* (Elsevier, Amsterdam, Netherlands, 1961), Vol. 2.

[104] J. Schlienz and G. Mahler, Description of entanglement, Phys. Rev. A **52**, 4396 (1995).